PAPER

Ion temperature profile stiffness: non-linear gyrokinetic simulations and comparison with experiment

To cite this article: J. Citrin *et al* 2014 *Nucl. Fusion* **54** 023008

IOP Publishing | International Atomic Energy Agency Nuclear Fusion
Nucl. Fusion **54** (2014) 023008 (18pp) doi:10.1088/0029-5515/54/2/023008

Ion temperature profile stiffness: non-linear gyrokinetic simulations and comparison with experiment

J. Citrin[1,4], F. Jenko[2], P. Mantica[3], D. Told[2], C. Bourdelle[4], R. Dumont[4], J. Garcia[4], J.W. Haverkort[1,5], G.M.D. Hogeweij[1], T. Johnson[6], M.J. Pueschel[7] and JET-EFDA contributors[a]

JET-EFDA, Culham Science Centre, Abingdon, OX14 3DB, UK
[1] FOM Institute DIFFER–Dutch Institute for Fundamental Energy Research, Association EURATOM-FOM, Trilateral Euregio Cluster, PO Box 1207, 3430 BE Nieuwegein, The Netherlands
[2] Max Planck Institute for Plasma Physics, EURATOM Association, Boltzmannstr. 2, 85748 Garching, Germany
[3] Istituto di Fisica del Plasma 'P. Caldirola', Associazione Euratom-ENEA-CNR, Milano, Italy
[4] CEA, IRFM, F-13108 Saint Paul Lez Durance, France
[5] Centrum Wiskunde and Informatica (CWI), PO Box 94079, Amsterdam, The Netherlands
[6] Euratom-VR Association, EES, KTH, Stockholm, Sweden
[7] Department of Physics, University of Wisconsin-Madison, Madison, WI 53706, USA

E-mail: J.Citrin@differ.nl

Received 28 August 2013, revised 14 November 2013
Accepted for publication 4 December 2013
Published 3 February 2014

Abstract

Recent experimental observations at JET show evidence of reduced ion temperature profile stiffness. An extensive set of nonlinear gyrokinetic simulations are performed based on the experimental discharges, investigating the physical mechanism behind the observations. The impact on the ion heat flux of various parameters that differ within the data-set are explored. These parameters include the safety factor, magnetic shear, toroidal flow shear, effect of rotation on the magnetohydrodynamic equilibrium, R/L_n, β_e, Z_{eff}, T_e/T_i, and the fast-particle content. While previously hypothesized to be an important factor in the stiffness reduction, the combined effect of toroidal flow shear and low magnetic shear is not predicted by the simulations to lead to a significant reduction in ion heat flux, due both to an insufficient magnitude of flow shear and significant parallel velocity gradient destabilization. It is however found that nonlinear electromagnetic effects due to both thermal and fast-particle pressure gradients, even at low β_e, can significantly reduce the ion heat flux, and is a key factor in explaining the experimental observations. A total of four discharges are examined, at both inner and outer radii. For all cases studied, the simulated and experimental ion heat flux values agree within reasonable variations of input parameters around the experimental uncertainties.

Keywords: tokamak transport, gyrokinetic simulation, electromagnetic turbulence

(Some figures may appear in colour only in the online journal)

1. Introduction

It is well established that one of the primary limitations of tokamak core energy confinement is ion-Larmor-radius-scale turbulent transport driven by background pressure gradients [1]. The ion-temperature-gradient (ITG) instability in particular has been long identified as a ubiquitous unstable mode in tokamak plasmas [2–4], and is primarily responsible for ion heat losses. The instability saturates in a nonlinear state in conjunction with nonlinearly excited zonal-flows, forming a self-organized turbulent system which sets the transport fluxes [5]. Ion temperature gradient modes are driven linearly unstable by logarithmic ion temperature gradients above a critical threshold, i.e., by $R/L_{Ti} > R/L_{Ti,\mathrm{crit}}$, where the tokamak major radius R is a normalizing factor. In the following, we term ion temperature profile 'stiffness' as the degree of sensitivity of the ion heat flux to the driving R/L_{Ti}.

[a] See the appendix of Romanelli F. *et al* 2012 *Proc. 24th IAEA Fusion Energy Conf. 2012 (San Diego, CA, 2012)* www-naweb.iaea.org/napc/physics/FEC/FEC2012/papers/197_OV13.pdf.

This definition is related to that of incremental diffusivity. At lower stiffness, higher R/L_{Ti} is attained for the same input heat flux and critical threshold.

It has been recently observed in dedicated experiments at JET that ion temperature profile stiffness can be reduced at low normalized radii ($r/a < 0.5$) [6–8]. This has been hypothesized to be related to the correlation between low magnetic shear ($\hat{s}$) and increased flow shear in the low-stiffness discharges. The observations concentrated on $\rho = 0.33$ and $\rho = 0.64$ (where ρ is the normalized toroidal flux coordinate). At $\rho = 0.33$, the stiffness is observed to transit from high to low when the flow shear was increased. However, at $\rho = 0.64$, stiffness is observed to be high irrespective of flow shear. A previous nonlinear gyrokinetic study based on the recent JET discharges at $\rho = 0.33$, as detailed in [7], reported only an ITG threshold shift with rotation, as opposed to a decrease in stiffness as observed. Additional observations made in [6–8] pertinent to this work are as follows: at low rotation at $\rho = 0.33$, the observed stiffness level is higher than the gyrokinetic simulation predictions; furthermore, the observed ITG threshold is lower than the nonlinear gyrokinetic prediction, questioning the manifestation of the Dimits shift [9] predicted by nonlinear simulations.

In this paper, we extend this previous work and investigate whether the experimental observations can be understood through nonlinear gyrokinetic modelling. Understanding these effects could allow the identification of a potential actuator for core T_i control. As opposed to the previous simulation work, we include numerical geometry, electromagnetic effects, fast ions, parallel velocity gradient (PVG) destabilization, and explore the impact of reasonable variations in input parameters (from the experimental data) such as safety factor (q), magnetic shear ($\hat{s}$), and R/L_n. For the analysis, linear and nonlinear simulations are carried out with the GENE code [10]. Four JET discharges (with the previous carbon wall) were selected: 70084, 66130, 66404 and 73221. Discharges 66130 and 66404 are situated on the 'high-rotation, low-stiffness branch' at $\rho = 0.33$ seen in figure 1 in [7], and partially reproduced here for convenience in figure 1. We note that discharge 66404 has also been analysed in [11], where the possibility of increased critical threshold in conjunction with the lowered stiffness is not ruled out. Discharge 70084 is a low flux, low-rotation discharge selected to provide a data point near the turbulence threshold. Discharge 73221 is a high flux, low-rotation discharge situated on the 'low-rotation, high-stiffness branch' at $\rho = 0.33$, as shown in figure 1. The specific questions which we investigate are the following:

(1) Is the experimentally observed stiffness reduction for the high-rotation discharges at $\rho = 0.33$ consistent with gyrokinetic nonlinear simulation predictions? Which plasma parameters have the highest impact on the stiffness level for ITG turbulence? Is there sufficient leeway in the plasma parameters due to uncertainties such that the experimental observations and nonlinear simulation predictions can be reconciled?
(2) Can the seeming high stiffness in the 'low-rotation, high-stiffness' branch at $\rho = 0.33$ be reconciled with the nonlinear simulations, given reasonable uncertainties in plasma parameters?
(3) At $\rho = 0.64$, is the *lack* of experimentally observed stiffness reduction for the high-rotation discharges consistent with gyrokinetic nonlinear simulation predictions?
(4) Can the experimentally extrapolated turbulence threshold be reconciled with the nonlinear turbulence threshold including the Dimits shift, given reasonable uncertainties in the plasma parameters?

The discharges were reanalysed with the CRONOS suite of integrated modelling codes [12] to identify any differences in parameters apart from rotation and R/L_{Ti} within the chosen discharge set—such as T_e/T_i, Z_{eff}, R/L_n, β_e, q, $\hat{s}$, and fast-particle content—that may lead to the observed differences in ion heat flux and R/L_{Ti}. The sensitivity of the ion heat flux and stiffness to these parameters was tested with GENE in dedicated R/L_{Ti} scans. Finally, complete simulations—i.e. collisional, electromagnetic, multi-species, and with rotation—were carried out at both $\rho = 0.33$ and $\rho = 0.64$.

For all cases studied, at both $\rho = 0.33$ and $\rho = 0.64$, the simulated and experimental ion-heat-flux values were found to agree within reasonable variations of input parameters around the experimental uncertainties. Regarding questions (2) and (4) above, we find that the nonlinear simulations are consistent with the experimental observations, within the uncertainties of the plasma parameters.

The key factor for explaining the experimental observations at $\rho = 0.33$ was found to be nonlinear electromagnetic stabilization of ITG turbulence due to both thermal and fast-particle pressure gradients. In previous linear gyrokinetic analysis, electromagnetic stabilization of ITG modes has been invoked as a possible factor in improved hybrid scenario confinement at ASDEX Upgrade and DIII-D, particularly at outer radii (i.e. beyond half radius) [13]. The increased nonlinear electromagnetic stabilization reported here may point to an even greater importance of this effect than previously recognized. In addition, suprathermal pressure fractions are typically higher in hybrid scenarios compared with 'standard' scenarios, owing to lower density due to lower current. Thus, these results indicate a more favourable extrapolation of hybrid scenarios to burning (DT) plasma regimes.

The rest of the paper is organized as follows. In section 2 the GENE gyrokinetic code is briefly reviewed, as are the base parameters of the simulated discharges. Section 3 discusses the stiffness sensitivity study at $\rho = 0.33$. Section 4 shows the full comparison between the ion-heat-flux measurements and gyrokinetic predictions at $\rho = 0.33$. In section 5 the same comparison at $\rho = 0.64$ is shown. Conclusions are presented in section 6.

2. GENE simulations and discharge parameters

GENE solves the gyrokinetic Vlasov equation, coupled self-consistently to Maxwell's equations, within a δf formulation [14]. Computational efficiency is gained by solving in field line coordinates. x is the radial coordinate, z is the (poloidal) coordinate along the field line, and y is the binormal coordinate. Both an analytical circular geometry model (derived in [15]) as well as a numerical geometry were used in this work. The circular geometry model avoids the order $\epsilon = a/R$ inconsistency present in the often applied s–α model, but does not include a Shafranov shift. For

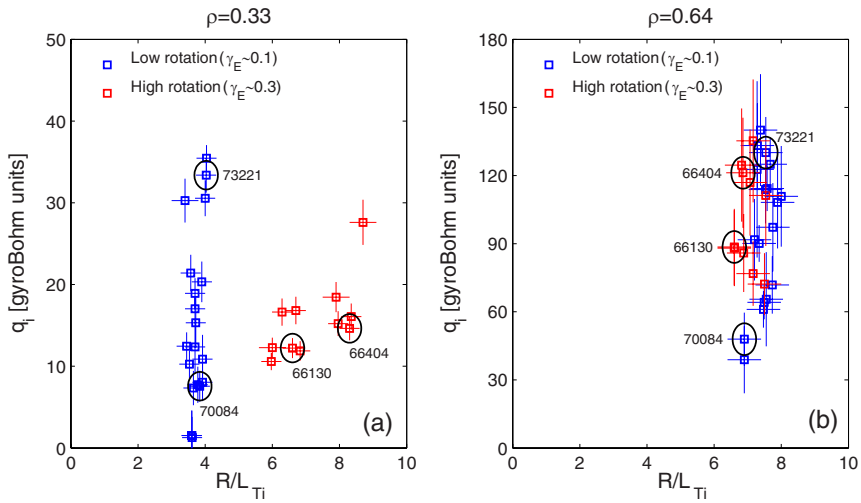

Figure 1. Partial reproduction of data presented in [7] displaying the separation between high and low-stiffness regimes at $\rho = 0.33$ (a) for discharges with low- and high-rotation respectively. At $\rho = 0.64$ (b) no significant separation of the stiffness behaviour is evident. The heat fluxes are in gyroBohm normalized units, $q_{GB} = T_i^{2.5} n_i m_i^{0.5} / e^2 B^2 R^2$. The specific discharges studied in this paper have been circled.

Table 1. Discharge dimensional parameters. The values are averaged between 9.5 and 10.5 s for discharges 70084 and 66130, between 6.5 and 7.5 s for discharge 66404, and between 7 and 8 s for discharge 73221. Quoted errors are statistical, and do not include possible systematic errors.

Shot no.@location	B (T)	I_p (MA)	T_i (keV)	T_e (keV)	n_e (10^{19} m^{-3})
70084@$\rho = 0.33$	3.5	1.8	2.01 ± 0.02	2.16 ± 0.1	2.6 ± 0.2
66130@$\rho = 0.33$	3.1	1.5	2.58 ± 0.04	3.3 ± 0.3	3.37 ± 0.24
66404@$\rho = 0.33$	3.5	1.8	3.1 ± 0.13	3.61 ± 0.08	2.3 ± 0.1
73221@$\rho = 0.33$	3.5	1.8	1.84 ± 0.04	2.44 ± 0.03	2.45 ± 0.16
70084@$\rho = 0.64$	3.5	1.8	1.08 ± 0.02	1.27 ± 0.05	2.3 ± 0.3
66130@$\rho = 0.64$	3.1	1.5	1.38 ± 0.03	1.5 ± 0.24	2.8 ± 0.3
66404@$\rho = 0.64$	3.5	1.8	1.34 ± 0.08	1.66 ± 0.14	1.51 ± 0.07

the numerical geometry, the FINESSE code was used to solve the extended Grad–Shafranov equation including toroidal rotation [16]. All simulations carried out were local, which is justified since $1/\rho^* \sim 500$ for the range of plasma parameters studied here [17, 18]. Both linear and nonlinear simulations were performed. In the linear mode, an eigenvalue solver was used to compute multiple modes for each point in parameter space [19, 20]. In the presence of rotation, when no time-independent eigenmodes can form, a complementary initial value solver was used.

Four discharges from the data-set presented in [7] were analysed at $\rho = 0.33$ and $\rho = 0.64$, where ρ is the normalized toroidal flux coordinate. The discharges are 70084, 66130, 66404 and 73221. 73221 is a high flux, low-rotation discharge situated on the 'low-rotation, high-stiffness branch' at $\rho = 0.33$, as shown in figure 1. The kinetic profiles of the four discharges were spline fitted and interpretative runs were carried out with the CRONOS integrated modelling suite of codes [12] for the equilibrium calculations and q-profile calculations. The kinetic profiles were then averaged over 1 s centred around 10/10/7/7.5 s respectively for calculations of the gradient lengths and other quantities such as β_e. The parameters are shown in tables 1 and 2. Discharge 73221 was only analysed at $\rho = 0.33$, for the investigation of the seemingly high stiffness of the low-rotation branch. The $\langle Z_{eff} \rangle$ values correspond to Bremsstrahlung measurements. Since the precise Z_{eff} profiles are not known, the sensitivity of the transport predictions to the range of reasonable Z_{eff} at $\rho = 0.33$ is explored in section 4. ν^* is the normalized collisionality: $\nu^* \equiv \nu_{ei} \frac{qR}{\epsilon^{1.5} v_{te}}$, with $\epsilon = a/R$ and $v_{te} = \sqrt{\frac{T_e}{m_e}}$. Note that the data presented in table 2 was processed *separately and independently* from the values quoted in [6, 7] and shown in figure 1. The R/L_{Ti} values in table 2 and figure 1 agree within error bars.

The agreement between the q-profiles obtained by CRONOS interpretative simulations and the measured q-profiles is satisfactory, as seen in figure 2. The average discrepancy between the interpretative and measured q-profile values at $\rho = 0.33$ and 0.64 is ~10%, within the estimated uncertainty of the q-profile measurements. The experimental q-profiles were obtained by EFIT constrained by either Faraday rotation measurements (discharges 70084 and 73221) or motional Stark effect (MSE) measurements (discharges 66130 and 66404).

In the GENE simulations, typical grid parameters were as follows: perpendicular box sizes $[L_x, L_y] = [170, 125]$ in units of $\rho_s \equiv c_s / \Omega_{ci} = \sqrt{T_e/m_i}/(eB/m_i)$, perpendicular grid discretizations $[n_x, n_y] = [192, 48]$, 24 point discretization in the parallel direction, 32 points in the parallel velocity direction, and 8 magnetic moments. Extensive convergence tests were carried out for representative simulations throughout

Table 2. Discharge dimensionless parameters. The $\hat{s}$ and q values are calculated by CRONOS interpretative simulations, assuming neoclassical diffusion. The values are averaged between 9.5 and 10.5 s for discharges 70084 and 66130, between 6.5 and 7.5 s for discharge 66404, and between 7 and 8 s for discharge 73221. Quoted errors are statistical, and do not include possible systematic errors.

Shot no.@location	$\hat{s}$	q	T_e/T_i	R/L_{Ti}	R/L_{Te}	R/L_{ne}	β_e (%)	ν^*	$\langle Z_{eff}\rangle$	$M[v_{tor}/c_s]$
70084@$\rho = 0.33$	0.7	1.7	1.08 ± 0.04	3.5 ± 0.5	3.8 ± 0.6	1.4 ± 0.4	0.19 ± 0.01	0.07	2.2 ± 0.1	0.09
66130@$\rho = 0.33$	0.7	1.8	1.25 ± 0.13	6 ± 0.4	6.5 ± 1	2.4 ± 1	0.46 ± 0.09	0.04	1.8 ± 0.1	0.31
66404@$\rho = 0.33$	0.4	1.8	1.14 ± 0.06	8.6 ± 0.9	5.5 ± 0.8	3.8 ± 0.4	0.35 ± 0.07	0.02	2.2 ± 0.1	0.19
73221@$\rho = 0.33$	0.7	1.5	1.33 ± 0.02	3.8 ± 0.4	5.4 ± 0.2	2.8 ± 0.3	0.2 ± 0.02	0.055	2.2 ± 0.1	0.07
70084@$\rho = 0.64$	1.3	3	1.18 ± 0.05	7.2 ± 0.2	6.4 ± 1	1.8 ± 0.8	0.096 ± 0.01	0.16	2.2 ± 0.1	0.03
66130@$\rho = 0.64$	1.5	3.5	1.1 ± 0.2	6.8 ± 0.3	8.5 ± 3	1.8 ± 1.4	0.18 ± 0.04	0.1	1.8 ± 0.1	0.23
66404@$\rho = 0.64$	1.4	2.9	1.23 ± 0.13	6.9 ± 0.4	10 ± 1.6	2.1 ± 0.9	0.08 ± 0.01	0.05	2.2 ± 0.1	0.15

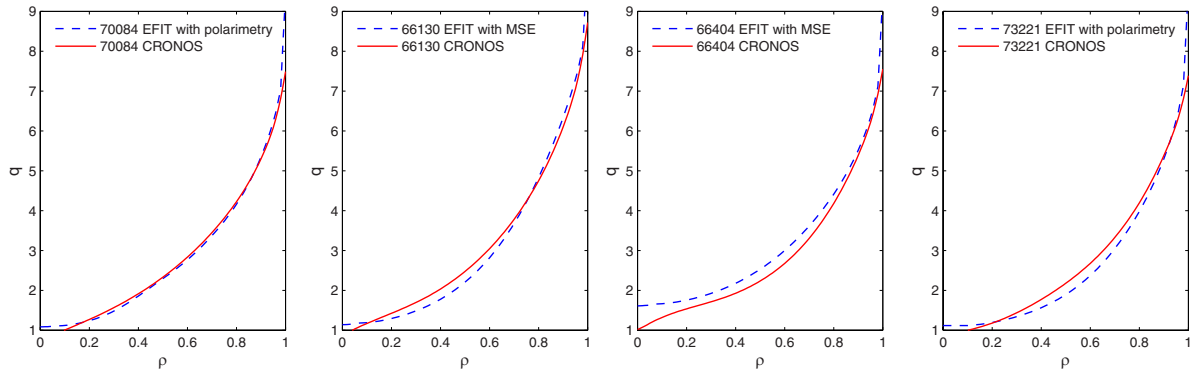

Figure 2. Comparison between CRONOS interpretative simulation q-profiles and experimental q-profiles. The profiles are averaged between 9.5 and 10.5 s for discharges 70084 and 66130, between 6.5 and 7.5 s for discharge 66404, and between 7 and 8 s for discharge 73221.

the parameter space spanned in this work. The lack of convergence of the heat fluxes with increasing n_y as reported for GYRO [21] simulations of discharge 70084 in [7]—associated with increasing zonal flows—was not encountered here. In our cases the convergence with n_y was well behaved. The difference may stem from the different treatment of the radial boundary conditions in these specific GENE and GYRO simulations. Further investigation is necessary to ascertain this. The heat fluxes shown in the following sections are in gyroBohm normalized units, $q_{GB} = T_i^{2.5} n_i m_i^{0.5}/e^2 B^2 R^2$. k_y is in units of $1/\rho_s$. These heat fluxes correspond to time averaged values over the saturated state of the GENE simulations. The statistical flux variations due to intermittency are for clarity not explicitly shown as error bars. This variation is typically 5–10% for our parameters. γ and γ_E are in units of c_s/R where $c_s \equiv \sqrt{T_e/m_i}$. All rotation is considered to be purely toroidal unless specifically mentioned otherwise. For the low- and high-rotation discharges $\gamma_E = 0.1$ and 0.3 respectively, at both $\rho = 0.33$ and $\rho = 0.64$. These are representative γ_E values for the low- and high-stiffness discharges from the dataset in [7].

3. Stiffness study at inner radius $\rho = 0.33$

In this section, we isolate the effect of various parameters on ion profile stiffness and critical threshold, at $\rho = 0.33$ (where the transition to low stiffness at high-rotation was observed). These parameters are: q, $\hat{s}$, rotation, effect of rotation on the magnetohydrodynamic (MHD) equilibrium, fast ion content, R/L_n, β_e and Z_{eff}.

3.1. Stiffness and threshold sensitivity to q and $\hat{s}$

While the linear ITG turbulence threshold increases with $\hat{s}/q$ [22], the stiffness (i.e. the rate of change of the gyroBohm normalized ion heat flux with respect to R/L_{Ti}) decreases in nonlinear ITG simulations with both decreasing $\hat{s}$ (for $\hat{s} <\sim 0.7$) and decreasing q. The reduced stiffness for decreasing $\hat{s}$ at low-$\hat{s}$ has been shown to be correlated with increased coupling to zonal flows [23]. For decreasing q, the stiffness reduction is due to a decreased downshift (compared with the peak in the linear spectrum) in the peak wavenumber of the turbulence spectrum, indicating decreased correlation lengths [24–26]. These sensitivities are shown in figure 3. The stiffness level is shown to decrease for decreasing $\hat{s}$ at low-$\hat{s}$ at constant $q = 1.3$. We can also see that for both the $\hat{s}/q = 0.6/1.3$ and $\hat{s}/q = 1/2$ cases the turbulence threshold is similar while the stiffness is lower for the $\hat{s}/q = 0.6/1.3$ case, due to the decreased q.

We will deliberately make an optimistic assumption that $\hat{s}/q = 0.2/1.3$ throughout all the subsequent parameter scans carried out at $\rho = 0.33$ in this section. For the numerical geometry cases, this was done by modifying the current profile input into CRONOS such that at $\rho = 0.33$ values of $\hat{s}/q = 0.2/1.3$ were obtained following the solution of the Grad–Shafranov equation. The choice of assuming $\hat{s}/q = 0.2/1.3$ is to ensure that we are in a 'low-$\hat{s}$ regime', which has been hypothesized to be an important factor in the stiffness reduction, based on the observed correlation between low stiffness and low-$\hat{s}$ throughout the data set in [7].

The discussion of the sensitivity of the linear threshold to q brings us to an important point. In [6, 7], it was pointed out that the measured turbulence threshold of the low-rotation discharges in the data set were lower than the predicted

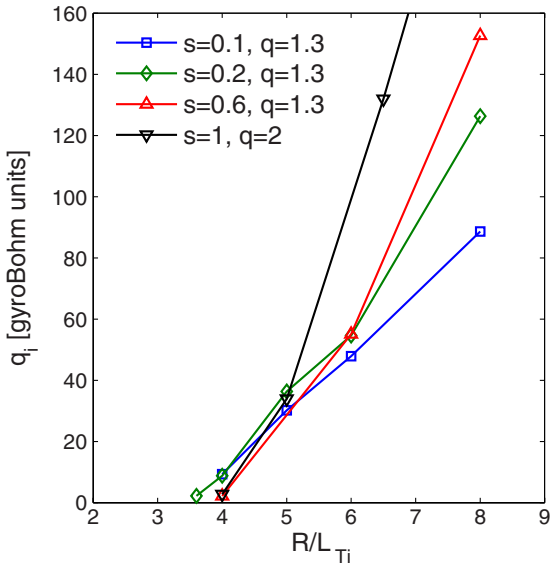

Figure 3. Nonlinear electrostatic collisionless GENE R/L_{Ti} scans for various levels of $\hat{s}$ and q-profile with circular geometry at $\rho = 0.33$. $R/L_{Te} = 5$, and $R/L_n = 1.1$.

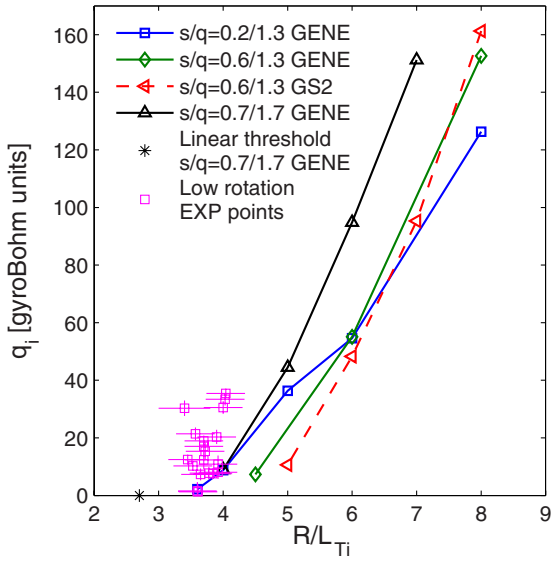

Figure 4. Comparison between nonlinear electrostatic collisionless GENE and GS2 R/L_{Ti} scans with the low-rotation data from the data-set in [7] for various levels of $\hat{s}$ and q. The GENE runs are with circular geometry at $\rho = 0.33$, the GS2 runs with $\hat{s} - \alpha$ geometry. $R/L_{Te} = 5$, and $R/L_n = 1.1$.

nonlinearly upshifted (Dimits shift) [9] thresholds. These thresholds were predicted by nonlinear simulations based on the low-rotation discharge 70084 performed with the GS2 nonlinear gyrokinetic code [27]. The measured turbulence thresholds agreed with the simulated linear thresholds as opposed to the nonlinear thresholds. This result thus questioned the Dimits shift paradigm. The q value used for these previous simulations was $q = 1.3$, based on the processed data at the time. However, the data processing methodology for obtaining q-profiles using Faraday rotation constraints at JET [28] has since been improved, leading to a revision of the measured q-profile value to $q = 1.7$ at $\rho = 0.33$ for $t \sim 10$ s for discharge 70084. The impact of this difference in q on the linear and nonlinear thresholds as predicted by the gyrokinetic codes is significant. This is shown in figure 4. In the figure, the GS2 predicted ion heat fluxes for the $\hat{s}/q = 0.6/1.3$ case (as shown in [6]) is compared with the analogous GENE simulations. The agreement between the codes is good, apart from the zone near the threshold. This difference is likely to be due to the different methods used to calculate the geometry: analytical circular in GENE, and $\hat{s} - \alpha$ geometry in GS2. However, the nonlinear threshold for $\hat{s}/q = 0.6/1.3$ in both codes is approximately $R/L_{Ti} \sim 4.5$, above the experimental threshold from [7]. These curves can then be compared with the R/L_{Ti} scan (carried out with GENE) with the revised, lower turbulence threshold corresponding to $\hat{s}/q = 0.7/1.7$. In this case, the linear threshold is $R/L_{Ti} = 2.7$, and the nonlinear threshold following the Dimits shift is at $R/L_{Ti} \sim 3.5$–4, in much better agreement with the experimental data. Consistency of the $\hat{s}/q = 0.7/1.7$ values with both the revised experimental q-profile and CRONOS simulations is thus suggestive that the Dimits shift paradigm is in fact now supported by the experimental observations. However, the high sensitivity of the turbulence thresholds to the precise $\hat{s}$ and q values leads us to a more conservative conclusion that no firm statement is justified regarding the consistency of the experimental data with the nonlinear Dimits shift. The various values of $\hat{s}$ and q used in the R/L_{Ti} scans in figure 4 (including the $\hat{s}/q = 0.2/1.3$ values subsequently used in this section) can be seen to constitute a sensitivity test of the 'reasonable' range of q and $\hat{s}$ in lieu of rigorous error bars. The one clear conclusion from this sensitivity scan, is that there is no clear *disagreement* between the experimental data and the nonlinear threshold upshifted due to the Dimits shift.

We note that the observed Dimits shift for the $\hat{s}/q = 0.7/1.7$ case is $\frac{\Delta(R/L_{Ti})}{R/L_{T\mathrm{crit}}} \approx 25\%$. This value is comparable with the $\frac{\Delta(R/L_{Ti})}{R/L_{T\mathrm{crit}}} \approx 20\%$ shifts observed in previous realistic simulations with kinetic electrons [29]. These shifts are significantly reduced compared with adiabatic electron simulations, where shifts of up to 50% are observed. The relatively low magnitude of the Dimits shift in simulations with realistic parameters illustrates that a definitive experimental observation of the effect may be extremely challenging, due to the error bars associated with the extrapolation to a critical turbulence threshold.

While the nonlinear turbulence threshold extrapolated from the $\hat{s}/q = 0.7/1.7$ curve in figure 4 matches the experimental threshold, the simulated stiffness level is seemingly lower than the experimental trend. The possibility that this discrepancy can be explained by the differences in T_e/T_i between the low flux and high flux points in the low-rotation branch—which impact the critical threshold—is explored in the more comprehensive simulations shown in section 4.1.

3.2. Stiffness sensitivity to rotation

In this subsection we isolate the effect of rotational flow shear on stiffness, assuming pure toroidal rotation. This assumption is justified for JET discharges with significant NBI. The application of flow shear is predicted to suppress

turbulence through two broad mechanisms: decorrelation of the turbulent structures in the nonlinear phase, once the shearing rate is comparable with or exceeds the inverse nonlinear autocorrelation time; and suppression of the driving linear modes by continuously shifting the mode from the most unstable spatial scale to nearby, more stable spatial scales [30, 31]. Nonlinear gyrofluid simulations with adiabatic electrons have predicted turbulence quenching above $\gamma_E/\gamma_{\max} = 1 \pm 0.3$ [32, 33], where for purely toroidal rotation the normalized $E \times B$ shear rate $\gamma_E \equiv \frac{r}{q}\frac{\mathrm{d}\Omega}{\mathrm{d}r}/(\frac{v_{\mathrm{th}}}{R})$, and $\gamma_{\max}$ is the maximum linear growth rate in the absence of rotation. Later gyrokinetic simulations, including cases with kinetic electrons, predicted that quenching occurs at somewhat higher (but similar) flow shear compared to the earlier gyrofluid simulations, at $\gamma_E/\gamma_{\max} = 2 \pm 0.5$ [34–36].

The abovementioned quench results were obtained in simulations which did not include a self-consistent PVG in the system, which can be destabilizing [37, 38]. When PVG destabilization is included, simulations have shown that it can limit the transport quench [32, 35, 39]. For pure toroidal rotation, the degree of the PVG destabilization depends on the magnetic geometry through the ratio q/ϵ. The PVG shear rate, γ_{p}, in the case of pure toroidal rotation, is such that $\gamma_{\mathrm{p}} = \frac{q}{\epsilon}\gamma_E$, where $\epsilon \equiv r/R$.

Collisionless, electrostatic simulations based on 70084 parameters (assuming $\hat{s}/q = 0.2/1.3$) are carried out, applying analytical circular geometry [15]. The predicted gyroBohm normalized ion heat fluxes from the R/L_{Ti} scans are shown in figure 5. The sensitivity to γ_E is examined when including (figure 5(*a*)) and neglecting (figure 5(*b*)) the contribution from PVG modes. Even for $\gamma_E = 0.6$, double the highest level of flow shear achieved in the reference data-set from [7], the simulated level of reduced stiffness is significantly less than the experimental observation, as seen by the direct comparison with the reference data. However, interesting effects related to the competition between stabilizing $E \times B$ shear and destabilizing PVG modes—particularly in the vicinity of the threshold—are observed. At low R/L_{Ti}, the PVG destabilization can dominate over the ITG turbulence, reducing stiffness in that region of parameter space. Due to the PVG destabilization, the fluxes do not continue to decrease towards the ITG instability thresholds. This is seen in figure 5(*a*) by examining the various curves at fixed R/L_{Ti}. At low R/L_{Ti}, the fluxes rise with γ_E due to PVG drive. However at higher R/L_{Ti}, the fluxes decrease with R/L_{Ti} due to the ITG stabilization by perpendicular $E \times B$ flow shear dominating over the PVG destabilization. In figure 5(*b*) the PVGs were artificially removed from the system, and the picture reverts to a threshold shift. Note that particularly for the (red) $\gamma_E = 0.3$ and (black) $\gamma_E = 0.6$ curves the apparent reduced slope near threshold is not necessarily indicative of reduced stiffness in that regime, since the actual effective nonlinear threshold may lie between the precise values of the R/L_{Ti} values chosen for the simulations.

For pure toroidal rotation, the relative importance of PVG destabilization versus $E \times B$ stabilization is sensitive to the geometric parameter q/ϵ (where $\epsilon \equiv r/R$) [40]. As q/ϵ increases, the field lines are increasingly projected onto the toroidal direction. In figure 6, a q/ϵ scan is carried out by varying ϵ in the various R/L_{Ti} scans. Simulations with $\epsilon = 0.11, 0.15$ assuming circular geometry were performed, as well as an $\langle\epsilon\rangle \equiv \langle r\rangle/R = 0.13$ case from the flux surface averaged minor radius at $\rho = 0.33$ using numerical geometry from the HELENA [41] equilibrium in the CRONOS simulation of discharge 70084. The R/L_{Ti} values in the plots corresponding to numerical geometry are defined here with respect to the averaged midplane minor radius. The relative strength of the PVG destabilization is seen to weaken as expected with decreasing q/ϵ, until an almost pure threshold shift case is reached with $q/\epsilon = 8.7$.

The interplay between PVG destabilization and $E \times B$ stabilization demands that PVG modes are correctly accounted for in reduced transport models—such as in gyrokinetic or gyrofluid based quasilinear models. Correct modelling near the turbulent thresholds is particularly critical for high temperature tokamaks, such as ITER. This is because the normalized fluxes are expected to be in the vicinity of the turbulence thresholds due to the $T_{\mathrm{i}}^{5/2}$ normalization dependence.

Finally, we note that the observed Dimits shift for these cases is only $\Delta(R/L_{Ti}) \approx 0.5$, or alternatively $\frac{\Delta(R/L_{Ti})}{R/L_{T\mathrm{crit}}} \approx 15\%$. This is another example of the relatively small Dimits shift observed in realistic simulations with kinetic electrons, as also shown in section 3.1 and in [29]. The linear threshold shown in figure 5 was calculated by extrapolation to zero-growth-rate of linear R/L_{Ti} scans with GENE. The linear threshold in the numerical geometry case is nearly identical to the circular geometry case.

In summary, the GENE simulations do not predict a significant reduction in stiffness due to flow shear, even with our deliberate choice of $\hat{s} = 0.2$. As suggested by figure 6(*c*) and as shown in section 4, a significant reduction of flux due to flow shear is only seen when both the effect of PVG destabilization is artificially reduced, and γ_E is increased beyond the experimental values expected from the toroidal flow shear.

3.3. Effect of rotation on the equilibrium.

In the previous section we examined the direct impact of rotation on the ion-heat-flux level through the flow shear. In this section we examine an indirect effect of rotation on the turbulent system through the impact of the centrifugal force on the plasma equilibrium. An extended Grad–Shafranov equation including toroidal rotation was solved with the FINESSE code [16], using the 70084 pressure and F profiles as input, where $F \equiv B_{\mathrm{tor}}R$. For the rotation profiles, scaled variants from 66404 were used such that static ($\gamma_E = 0$), $\gamma_E = 0.3$ and $\gamma_E = 0.6$ cases were studied. All values correspond to $\rho = 0.33$. The different equilibria are seen in figure 7. The sensitivity of the equilibria to these levels of rotation are found to be small, as expected due to the Mach number squared scaling of the 'rotation pressure'. Only a 10% increase in the Shafranov shift was observed between the static and $\gamma_E = 0.6$ case. The nonlinear predicted flux sensitivity to this different Shafranov shift is also minimal, with only a 6% decrease in ion heat flux when the $\gamma_E = 0.3$ equilibrium is used compared with the static equilibrium for a run with $R/L_{Ti} = 6.9$. We can thus conclude that the effect of rotation on the equilibrium itself can only play a minor role in setting the profile stiffness.

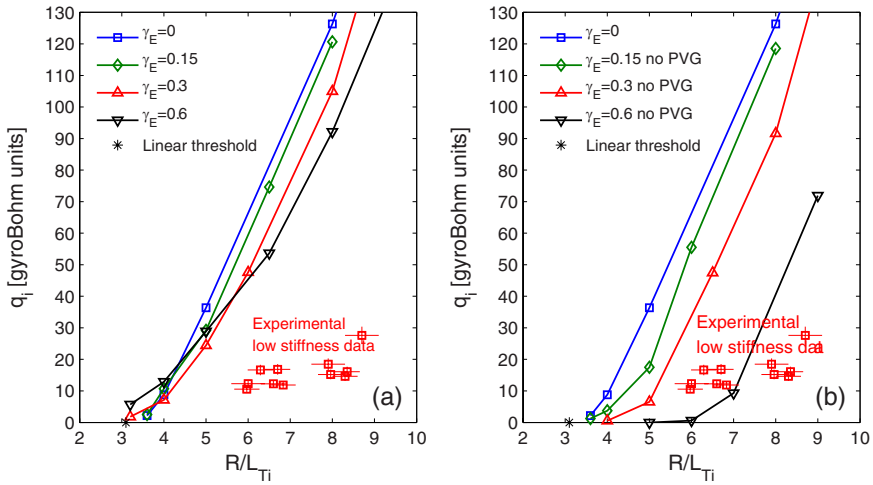

Figure 5. Nonlinear GENE R/L_{Ti} scans based on 70084 parameters at $\rho = 0.33$ ($q/\epsilon = 11.8$ for circular geometry) and various levels of γ_E [c_s/R]. Runs including PVG destabilization are shown in (a). Runs ignoring PVG destabilization are seen in (b). All runs were electrostatic, collisionless, and with circular geometry. The results are compared with the low-stiffness data at $\rho = 0.33$ from [7].

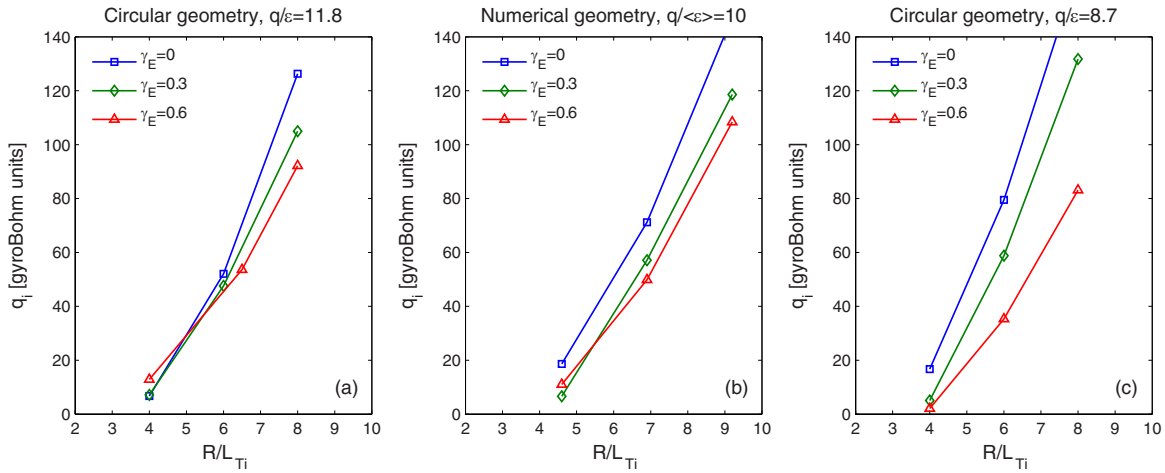

Figure 6. q/ϵ sensitivity of the PVG destabilization as seen in R/L_{Ti} scans of ion heat flux. As q/ϵ is progressively raised, the γ_E induced stabilization can not only be reduced but can even be reversed in the region of the instability threshold. Runs were electrostatic, collisionless, and with circular geometry.

3.4. Impact of R/L_n on the stiffness level

In the limited experimental data-set studied, there is a wide variation in R/L_n, from 1.4 in the 70084 case to 3.8 in the 66404 case (which corresponds to the highest R/L_{Ti} in the data-set). The sensitivity of the turbulence to the R/L_n value was thus examined. In particular, the possibility that nonlinear ITG-TEM (trapped electron mode) interplay takes place which can reduce the level of turbulence and thus the stiffness, as reported in [42], was investigated. In figure 8, these linear scans are shown. For $R/L_n = 1$, the dominant mode propagates in the ion diamagnetic direction (ITG mode). However, for $R/L_n = 3.8$ the mode at low R/L_{Ti} propagates in the electron diamagnetic direction. This is most probably a density gradient driven TEM mode, which is stabilized by R/L_{Ti} (which would correspond to low stiffness) until it switches to an ITG mode at $R/L_{Ti} \approx 5$. At that point we would expect turbulence stabilization according to [42]. However, for higher R/L_{Ti} the growth-rate stiffness is similar to the $R/L_n = 1$ case, as a pure ITG regime is reached. For $R/L_n = 5$ the TEM-dominated regime is maintained for much higher R/L_{Ti}. However, the highest experimental R/L_n in the data-set of [7] is $R/L_n \approx 4$. Furthermore, at the experimental high R/L_{Ti} values the transport is ITG dominated and stiff even for $R/L_n = 5$. Thus it is unlikely that R/L_n is responsible for reduced profile stiffness. Furthermore, even if the stiffness is low, the actual growth rates themselves are high, and we may expect a high degree of transport.

These results are maintained in the nonlinear scans, seen in figure 9. While at lower R/L_{Ti} stiffness is indeed reduced in the TEM regime for the high R/L_n case, at higher R/L_{Ti} values the difference in stiffness between the $R/L_n = 1$ and $R/L_n = 3.8$ cases becomes negligible. We can conclude that the variance of R/L_n in the data-set is not responsible for the observed difference in stiffness.

3.5. Impact of $Z_{\rm eff}$ and $T_{\rm e}/T_{\rm i}$

The effect of $Z_{\rm eff}$—which is stabilizing for ITG turbulence for impurity density gradients with the same sign as the

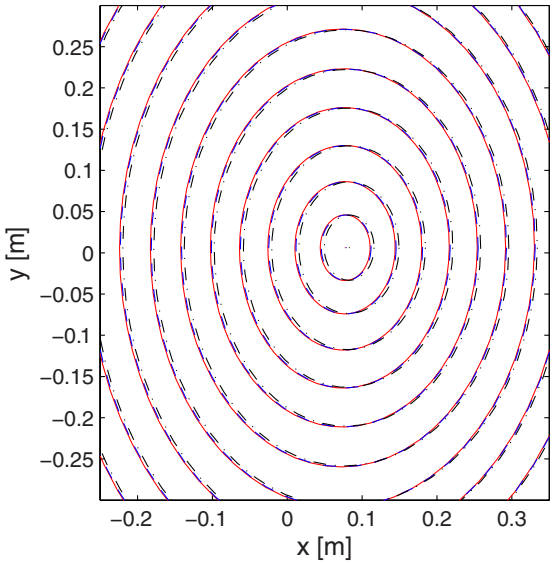

Figure 7. Flux surfaces in the vicinity of the magnetic axis from a solution of the generalized Grad–Shafranov equation using the kinetic profiles of 70084 and scaled rotation profiles from 66404. Three cases are shown: static (red solid curves), $\gamma_E = 0.3$ (blue dashed curves) and $\gamma_E = 0.6$ (black dashed–dotted curves).

main ion density gradient—was modelled in the three-species simulations by lumping all impurities into a kinetic fully stripped carbon ion species. The carbon temperature, R/L_T, and R/L_n were assumed the same as the main deuterium species. Simulations with varying $Z_{\rm eff}$ values were carried out, to test the sensitivity of the predictions to the uncertainties in the $Z_{\rm eff}$ profile shape. The growth-rate sensitivity to $Z_{\rm eff}$ and $T_{\rm e}/T_{\rm i}$ for linear GENE runs based on discharge 66404 can be seen in figure 10. For our cases, the $Z_{\rm eff}$ stabilization tends to be compensated by the $T_{\rm e}/T_{\rm i} > 1$ destabilization. In nonlinear simulations, assuming $R/L_{Tc} = 0$ for the carbon species instead of $R/L_{Tc} = R/L_{Ti}$ altered the bulk ion heat flux by less than 2%.

The *differences* in $Z_{\rm eff}$ and $T_{\rm e}/T_{\rm i}$ between the various discharges—within the statistical errors of these parameters—are insufficient for $Z_{\rm eff}$ and $T_{\rm e}/T_{\rm i}$ to solely explain the stiffness reduction. However, the sensitivity of the growth rates to these parameters is sufficient such that we cannot neglect the possibility of systematic errors leading to systematic discrepancies between the ion heat flux simulations and measurements. This is explored in nonlinear $Z_{\rm eff}$ sensitivity studies in section 4.2.

3.6. Inclusion of fast particles

The discharges studied are relatively low density cases. This allows for the sustainment of a significant fraction of non-thermalized fast ions in the plasma, particularly for the higher rotation cases, where significant NBI is employed. The impact of these fast ions on the ion heat flux is investigated in this section. The presence of fast ions is in general predicted to reduce the turbulent drive through a number of mechanisms. One such mechanism is the dilution of the main ion species by the fast ions. In ASDEX Upgrade strong evidence has pointed to a fast ion dilution mechanism for internal transport barrier (ITB) formation at low density [43]. Additionally, a geometric stabilization mechanism exists—particularly relevant at low-$\hat{s}$—whereby the increased Shafranov shift induced by increased $\alpha \equiv \beta' q^2 R$ modifies the drift frequencies and reduces the drive of ITG instabilities [44]. Finally, an increase in local α due to fast ion suprathermal pressure gradients also stabilizes ITG modes through electromagnetic effects. This *electromagnetic* α-stabilization is distinct and unrelated to the aforementioned *geometric* α-stabilization. This mechanism has been suggested as a trigger for ITB formation in low density JET hybrid discharges [45]. A fast ion fraction has been previously proposed to be responsible for mismatch between gyrokinetic simulations and experiments [46]. In this section we investigate the linear impact of the dilution and electromagnetic effects. The impact of the Shafranov shift effect is also investigated here nonlinearly.

Monte Carlo simulations of the NBI injection and subsequent fast ion slowing down were carried out for discharge 66404 with NEMO/SPOT [47] within the CRONOS integrated modelling framework. An average fast-particle energy (≈35 keV) at $\rho = 0.33$ was calculated. In the GENE simulations, the fast-particle temperature was approximated to the average fast-particle energy value. Approximating the fast-particle slowing-down distribution as a Maxwellian is not strictly justified. However, the high energies (compared to the main ions) of the fast particles leads to a significant proportion of the fast particles having Larmor radii greater than the typical turbulent eddy scale lengths. This then decreases the backreaction of the fast tail on the system. However, a dedicated study of the impact of various fast-particle distribution functions on the turbulent system is necessary to fully justify this assumption.

A linear GENE scan of fast particle densities (relative to $n_{\rm e}$) can be seen in figure 11. The scan is carried out for various k_y values in figure 11(*a*). The scans assume $R/L_{T\rm fast} = R/_{n\rm fast} = 0$—equivalent to assuming pure ion dilution. The $R/L_{n\rm fast}$ sensitivity is examined in figure 11(*b*) at $k_y = 0.4$. Increasing $R/L_{n\rm fast}$ corresponds to an increased pressure gradient, increasing the stabilization through electromagnetic effects as expected. The modelled fast ion pressure gradient at $\rho = 0.33$ corresponds to $R/L_{n\rm fast} = 15$. A suppression of the growth rates is observed with increasing $n_{\rm fast}/n_{\rm e}$. However, for discharge 66404 (high rotation, low-stiffness case), the fast ion fraction is predicted by NEMO/SPOT to be only ∼10%. Interpolating to $R/L_{n\rm fast} = 15$, this corresponds to a growth-rate reduction of ∼15%. According to the linear simulations, this magnitude is insufficient to explain the reduced stiffness.

The above analysis was carried out for the NBI fast ions. With regard to the ICRH fast ions, the effect of the ion dilution is indirectly taken into account in the full modelling described in section 4 by the higher $Z_{\rm eff}$ due to the ^{3}He minority. From SELFO [48] modelling, which includes finite ion cyclotron orbit width effects, important for an accurate calculation of the ICRH fast ion pressure profile width, we determined that the ICRH induced suprathermal pressure gradient is similar in magnitude to the NBI profile at $\rho = 0.33$ with a similar linear stabilization effect. However, we anticipate the results of section 3.7 and section 4 and state that the electromagnetic stabilization effect is enhanced nonlinearly, and is a key factor in explaining the observed stiffness reduction.

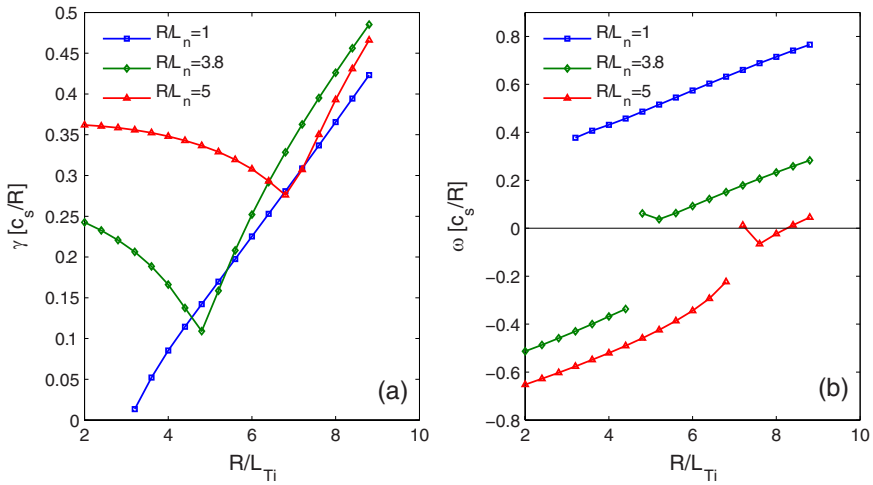

Figure 8. Linear R/L_{Ti} scans based on 66404 parameters at $\rho = 0.33$ with varying R/L_n. Growth rates are shown in (a), and frequencies in (b). Runs were electrostatic, with collisions, and with circular geometry.

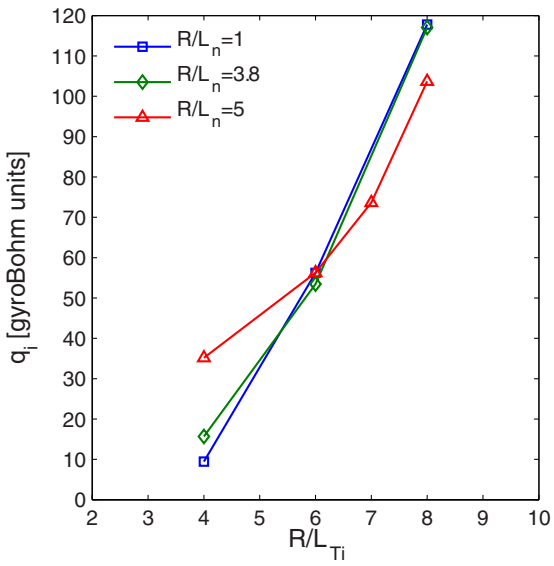

Figure 9. Nonlinear R/L_{Ti} scans based on 66404 parameters at $\rho = 0.33$ with varying R/L_n. Runs were electrostatic, with collisions, and with circular geometry.

In the above analysis, the influence of the suprathermal pressure on the magnetic geometry through an increased Shafranov shift was not taken into account. The increased Shafranov shift can be seen in figure 12, where the flux surfaces for the low power discharge 70084, and the high power discharge 66404 (with and without the inclusion of the NBI fast-particle pressure) are compared. The fast-particle contribution to the 66404 Shafranov shift is significant. For 70084, the Shafranov shift is ≈7.5 cm. For 66404 with the thermal pressure contribution only, the Shafranov shift is ≈8.8 cm. For 66404 with the total pressure (including fast particles), the total Shafranov shift is ≈13 cm. The impact of this difference on the predicted fluxes was investigated through dedicated nonlinear simulations. A flux reduction of 15% was observed in the nonlinear simulations with $R/L_{Ti} = 8$ when substituting the numerical geometry from 70084 with that of 66404 (i.e. with the fast-particle content), as seen in figure 13. While not negligible, the impact of the increased Shafranov shift cannot be the sole explanation for the reduction in stiffness observed.

3.7. Impact of β_e on the stiffness level

In this subsection the sensitivity of the stiffness on electromagnetic effects—which arise for $\beta_e > 0$—is examined. The simulations carried out take discharge 66404 parameters as a reference.

3.7.1. Modelling results. Linear (at $k_y = 0.4$) and nonlinear β_e scans are shown in figure 14. From the linear scans, it is clear that the range of experimental β_e values (0–0.5%) are significantly below the kinetic ballooning mode (KBM) thresholds, characterized in the plot by the sharp upturn in growth rates at $\beta_e \approx 1.5 - 2.4\%$; this finding is expected to carry over to the nonlinear physics [49]. Below the KBM threshold, β_e stabilizes the ITG mode [50, 51]. For our parameters, this leads to a growth-rate reduction of ≈25% at $\beta_e = 0.5\%$. This is at the upper range of our experimental β_e values. The 25% growth-rate stabilization factor is not exceeded when repeating the linear simulations for $k_y = 0.1$–0.3. The linear ITG mode is stabilized at lower and lower β_e as R/L_{Ti} is increased. This is likely due to the corresponding increase in $\alpha \equiv \beta' q^2 R$, which can be considered a parameter of merit for the strength of the electromagnetic coupling.

A striking observation is that the *nonlinear* β_e ITG stabilization significantly exceeds the linear stabilization. This is consistent with GENE results reported in [49, 52], and with other codes [53, 54]. A decrease in ion heat flux by a factor of 65% is seen in figure 14(b) for the $\gamma_E = 0$, $R/L_{Ti} = 9.2$ case between $\beta_e = 0$–0.48%. Simultaneously, while the ion heat flux is reduced by β_e in the $\gamma_E = 0$, $R/L_{Ti} = 4.6$ case, it is not totally quenched. The observation that for $\beta_e > 0$ the flux level is diminished over a range of R/L_{Ti}, yet is not totally quenched in the vicinity of the ITG threshold for $\beta_e = 0$, is indicative that $\beta_e > 0$ (within the range studied) induces a decrease in stiffness as opposed to a threshold shift. Note that the results reported in [52] cannot be compared with those in

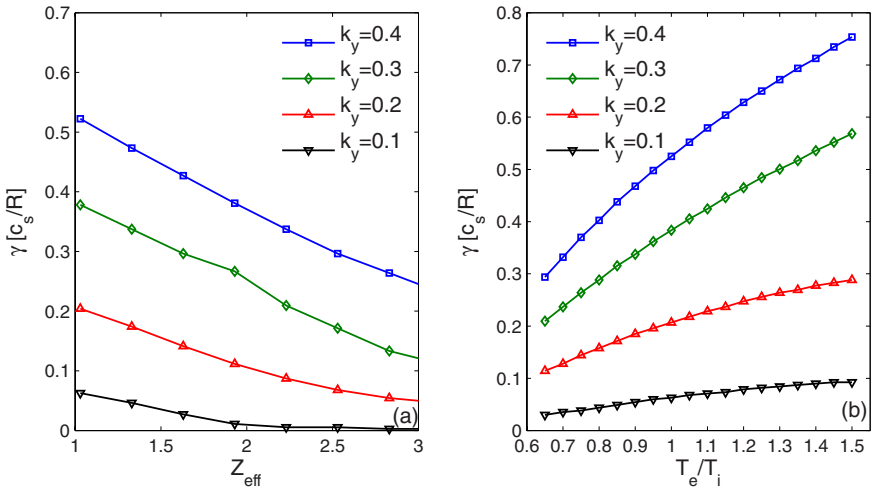

Figure 10. Sensitivity of growth rates to $Z_{\rm eff}$ (a) and $T_{\rm e}/T_{\rm i}$ (b) from linear GENE runs based on 66404 parameters at $\rho = 0.33$. Runs were electromagnetic, with collisions, and with numerical geometry.

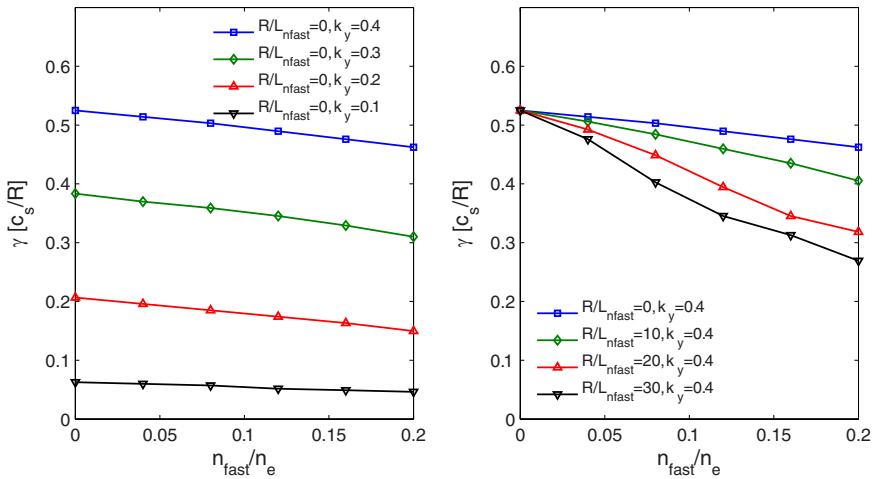

Figure 11. Linear fast-particle density scans with 66404 parameters at $\rho = 0.33$ at various values of k_y (left panel) and $R/L_{n\rm fast}$ (right panel). Runs were electromagnetic, with collisions, and with numerical geometry.

figure 14(b) quantitatively, as TEM contributions to the overall turbulence picture may change in particular the $\beta_{\rm e}$ dependence of the threshold shift.

It is interesting to note that the stabilizing effect of flow shear is weakened by finite $\beta_{\rm e}$ in the higher R/L_{Ti} case, as seen in figure 14. In the $R/L_{Ti} = 9.2$ case, the effect of flow shear on the turbulence switches from stabilizing to destabilizing as $\beta_{\rm e}$ increases. However, in the $R/L_{Ti} = 4.6$ case flow shear is always stabilizing, and no discernible weakening of the stabilization is seen as $\beta_{\rm e}$ increases. Linearly, the PVG modes are not observed to lead to increased destabilization at increased $\beta_{\rm e}$. More effort needs to be taken in the future to uncover the nonlinear effects which either increases PVG destabilization or decreases the $E \times B$ stabilization in the high R/L_{Ti} case.

We note that the electromagnetic stabilization is expected to be effective up to the recently discovered non-zonal-transition $\beta_{\rm e}$ limit [55], beyond which electromagnetic fluctuations effectively short out the zonal flows and lead to a significant increase in the saturated level of the ITG turbulent fluxes. This $\beta_{\rm e}$ threshold very strongly depends on the background gradients, however, and for typical (low) gradients quickly becomes less restrictive than the KBM threshold. Coupled with the fact that this effect produces a limit with enormous stiffness, it can therefore be expected that standard experimental gradient and $\beta_{\rm e}$ values lie below this point, putting those cases in the electromagnetic stabilization zone.

We can thus conclude that electromagnetic effects play a significant role in stiffness reduction for our parameters, even at relatively low values of $\beta_{\rm e}$. While this stiffness reduction is not sufficient to fully explain the experimentally observed stiffness reduction, it is a factor which must be taken into consideration. We note that the fast-particle stabilization observed in section 3.6 is also an electromagnetic ITG stabilization mechanism, and we can thus expect nonlinearly a greater impact of the fast-particle stabilization. This is explored in section 4.

3.7.2. Nonlinear electromagnetic stabilization mechanisms. In [49, 52], an increase of the ratio between the zonal flow shearing rate to the unstable mode growth rate ($\omega_{\rm ZF}/\gamma$) is observed with $\beta_{\rm e}$. This has been linked to an increase

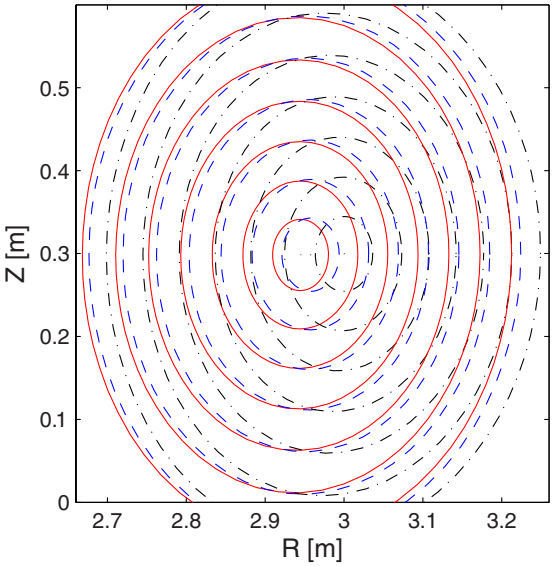

Figure 12. Flux surfaces in the vicinity of the magnetic axis for discharge 70084 (red solid curves), 66404 without fast-particle pressure, (blue dashed curves) and 66404 with the inclusion of fast-particle pressure (black dashed–dotted curves).

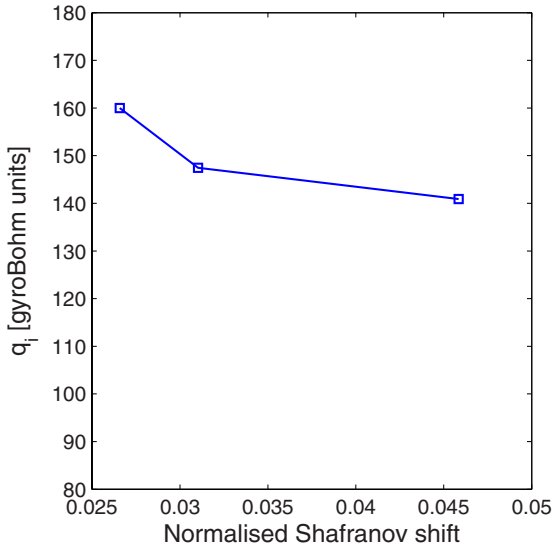

Figure 13. Flux reduction as a function of Shafranov shift normalized to the major radius for the three equilibria presented in figure 12.

in the zonal flow growth rate [56]. This is suggested to be part of the explanation of the nonlinearly enhanced β-stabilization. A possible physical mechanism for this relative increase in zonal flow activity, based on increased coupling between Alfvénic modes and drift waves, has also been suggested [57]. In figure 15 we plot the mode amplitude spectra for the $\gamma_E = 0$, $R/L_{Ti} = 9.2$ scan over β_e shown in figure 14. The amplitude spectra have been normalized to the zonal flow (or rather $k_y = 0$, which constitutes a reasonably good measure) amplitudes. Indeed, a relative increase in the $k_y = 0$ modes is seen for the electromagnetic cases, which may be related to the ITG β_e stabilization. A conjecture for the mechanism of increased zonal flow coupling is the observed widening of the ITG linear eigenmode structure observed with increasing β_e, as shown in figure 16. The less ballooned structure facilitates the direct coupling to the poloidally symmetric zonal modes, similarly to what occurs at low magnetic shear [23, 58]. Further work is suggested to shed more light on this topic.

4. Simulated and measured ion-heat-flux comparisons at $\rho = 0.33$

In the previous section we have analysed the individual impact of numerous parameters on ITG mode stabilization and ion temperature profile stiffness reduction. In this section we simultaneously include all effects—flow shear, the effect of rotation on equilibrium, experimental R/L_n, finite β, collisions, $Z_{\text{eff}} > 1$, and experimental T_e/T_i—and carry out realistic simulations of all four discharges in the data-set at $\rho = 0.33$. We analyse the 'high-stiffness-branch' and 'low-stiffness-branch' separately in sections 4.1 and 4.2 respectively. Ion heat fluxes from nonlinear simulations and experimental power balance are compared.

4.1. Investigation of the low-rotation, high-stiffness branch

In section 3.1, figure 4, it is evident that the stiffness of the simulated $\hat{s}/q = 0.7/1.7$ curve is less than the apparent experimental trend. In this section, we examine the possibility that the higher T_e/T_i of the high flux discharge 73221 in the low-rotation branch is responsible for the increased flux, through the T_e/T_i impact on the ITG critical threshold. It is important to note that this significant difference in T_e/T_i between the high and low flux discharges in the low-rotation branch has become apparent only recently after data reprocessing following an in-vessel calibration of the ECE diagnostic. This is the reason why this aspect was not taken into account in [6, 7].

An $R/L_{T\text{crit}} \propto (1 + T_i/T_e)$ scaling has been derived both analytically and from linear gyrokinetic simulations for the ITG instability [2, 22]. A decreased instability threshold leads to increased flux for a given R/L_{Ti} value, as long as the stiffness level does not change with T_e/T_i. It has been predicted by nonlinear simulations that the stiffness level is not highly sensitive to T_e/T_i within the range relevant for our studied discharges [59]. The simulation results for the 70084 and 73221 discharges are shown in figure 17. Since R/L_{Ti} is close to threshold and the transport is relatively stiff, the results are highly sensitive to the input parameters. Additionally, the proximity to threshold leads to statistical flux variations due to intermittency often higher than the typical 5–10% level observed for the simulations in this paper. These variations are displayed on the plot for these specific cases. For 70084, agreement between the nonlinear simulation and the experimental observation was found for reasonable departures from the base parameters recorded in table 2. R/L_{Ti} and T_e/T_i were both taken at the high end of their error bars. For the base values of R/L_{Ti} and T_e/T_i, stability was predicted. Z_{eff} was taken as 1.4, lower than $\langle Z_{\text{eff}} \rangle = 2.2$. This is a reasonable assumption since the Z_{eff} profiles tend to be hollow, and $\rho = 0.33$ is relatively close to the magnetic axis. Making the same assumptions

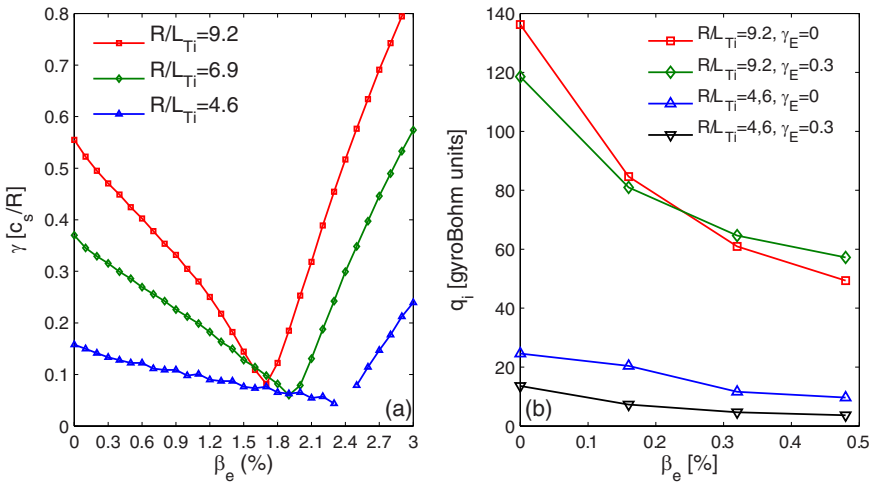

Figure 14. Linear (*a*) and nonlinear (*b*) β_e scans with 66404 parameters at $\rho = 0.33$. R/L_{Ti} and γ_E are varied. Runs were with collisions and numerical geometry.

for 73221 (although maintaining the base value of T_e/T_i), the simulated flux value was found to be significantly lower than the experimental value. Even though T_e/T_i is higher in 73221 than in 70084, the impact of the higher T_e/T_i on the ITG critical threshold is compensated by the lower q value calculated by the 73221 CRONOS interpretative simulation compared with 70084. However, when increasing the 73221 q value in the simulation to equal the 70084 value—an increase of only approximately 15%—the simulated flux value then becomes comparable to the experimental value. When assuming the Faraday rotation constrained EFIT q-profile for 73211, with $\hat{s}/q = 0.5/1.4$, we obtain an intermediate flux level between the 70084 and 73221 experimental flux values. These tests of the variation in the 73221 flux values with variations of q and $\hat{s}$ constitute a sensitivity analysis of the fluxes to reasonable estimates of the q-profile error bar. We thus deem that the T_e/T_i increase of the high flux cases in this branch compared with the low flux cases is a likely explanation for the seeming anomalously high stiffness of this data-set. However, the high sensitivity of the simulated flux—through the impact on the critical threshold—to T_e/T_i and the q-profile variations within the estimated experimental error bars precludes a firm conclusion on this point. The result lies within the uncertainties—particularly of the q-profile calculations. In table 3 we show the results for all simulations carried out for 70084 and 73221—beyond those shown in figure 17. The sensitivities of the flux to input parameters such as $\hat{s}$, q, $Z_{\rm eff}$, γ_E and R/L_n are shown. We note that the results are *not* highly sensitive to wide variations in the R/L_n values.

4.2. Investigation of the high-rotation, low-stiffness branch

The comparison between the GENE nonlinear simulations and the experimental heat fluxes for the 'low-stiffness branch' is shown in figure 18. For the high-rotation discharges, three separate sets of simulations are shown: with the nominal q-profile from the CRONOS interpretative runs and $Z_{\rm eff} = 1.9$, with the optimistic $\hat{s}/q = 0.2/1.3$ assumption and $Z_{\rm eff} = 1.9$, and finally with the optimistic $\hat{s}/q = 0.2/1.3$ assumption and $Z_{\rm eff} = 2.4$. Fast ions are not included in these simulations due to the added computational expense. The input parameters

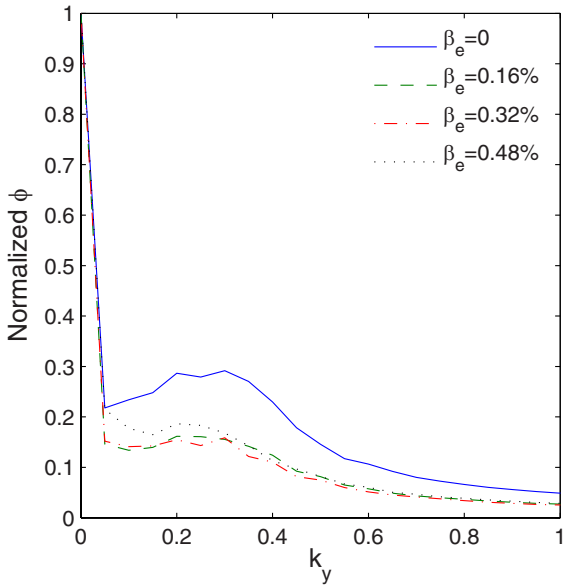

Figure 15. Amplitude spectra from the $\gamma_E = 0$, $R/L_{Ti} = 9.2$, nonlinear β_e scan displayed in figure 14(*b*).

and flux values for these simulations, as well as additional simulations carried out for further sensitivity studies and for clarity not shown in figure 18, are listed in table 4.

For the $R/L_{Ti} = 6$ discharge 66130, the simulation with the nominal parameters (i.e. with the CRONOS $\hat{s}$ and q values) leads to a flux value approximately $\times 2.5$ above the experimental level. This discrepancy can be reduced by a reasonable variation of input parameters around the experimental uncertainties, either for q and $\hat{s}$, $Z_{\rm eff}$ or R/L_{Ti}. However, the discrepancy between the simulation and the experimental flux for the higher $R/L_{Ti} = 8.6$ discharge—66404—is significantly greater. For the simulation with the base input parameters, the simulated flux is approximately $\times 5$ higher than the experimental value. The simulated and experimental flux can only be reconciled by making a highly optimistic assumption with regard to the simultaneous variation of R/L_{Ti}, $Z_{\rm eff}$, $\hat{s}$, q and T_e/T_i around their estimated error bars—as seen in the last line of table 4.

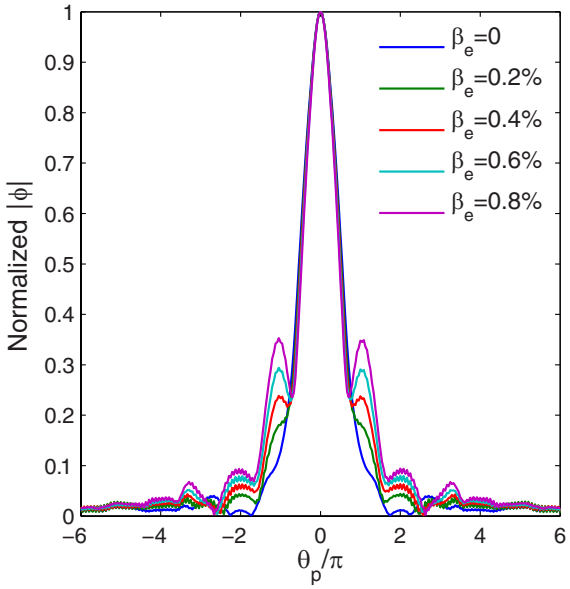

Figure 16. β_e scan of ITG eigenmode structure calculated by linear-GENE. $R/L_{Ti} = 9.2$, and $\gamma_E = 0$.

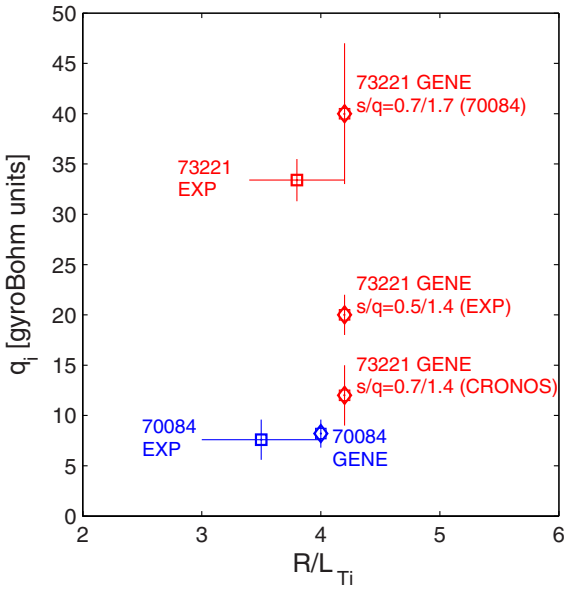

Figure 17. Comparison of experimental and simulated ion heat flux for discharges 70084 and 73221 situated on the 'high-stiffness-branch' at $\rho = 0.33$ from the dataset of [7]. The 73221 simulation results shown were carried out for three separate $\hat{s}/q$ values to test the sensitivity to the q-profile uncertainties.

The agreement between the simulations and measured flux values for 66404 can however be significantly improved by including the fast ion species as active species in the electromagnetic nonlinear gyrokinetic simulations, which is also consistent with the findings in [60]. The results are shown in figure 19, and are discussed in deeper detail in [61]. Briefly, at this radius, the fast ion induced suprathermal pressure gradient dominates the total pressure gradient, and augments significantly the electromagnetic stabilization discussed in section 3.7. With the combined contribution of the NBI and ICRH induced suprathermal pressure gradients, the calculated

Table 3. Input data and ion heat flux results for discharge 70084 and 73221 nonlinear simulations. The cases in bold font are the simulations displayed in figure 17.

Shot number	Z_{eff}	R/L_{Ti}	R/L_n	T_e/T_i	γ_E	$\hat{s}$	q	q_i (gyroBohm units)
70084	1.4	3.5	1.4	1.12	0.07	0.7	1.7	0
70084	1.4	4	1.4	1.12	0.1	0.2	1.3	0
70084	**1.4**	**4**	**1.4**	**1.12**	**0.1**	**0.7**	**1.7**	**8.2 ± 1.4**
70084	1.4	4	1.4	1.12	0.07	0.7	1.7	14 ± 4
70084	1.4	4	1.4	1.08	0.1	0.7	1.7	0
70084	1.9	4	1.4	1.12	0.07	0.7	1.7	0
70084	1.9	4	1.4	1.12	0.04	0.7	1.7	7.5 ± 1.5
73221	**1.4**	**4.2**	**2.8**	**1.35**	**0.02**	**0.7**	**1.4**	**12 ± 3**
73221	1.4	4.2	1.0	1.35	0.02	0.7	1.7	48 ± 2
73221	**1.4**	**4.2**	**2.8**	**1.35**	**0.02**	**0.7**	**1.7**	**40 ± 7**
73221	1.4	4.2	3.8	1.35	0.02	0.7	1.7	31 ± 7
73221	**1.4**	**4.2**	**2.8**	**1.35**	**0.02**	**0.5**	**1.4**	**20 ± 2**
73221	1.9	4.2	2.8	1.35	0.02	0.7	1.4	1.7 ± 0.3
73221	1.9	4.2	2.8	1.35	0.02	0.7	1.7	13 ± 3

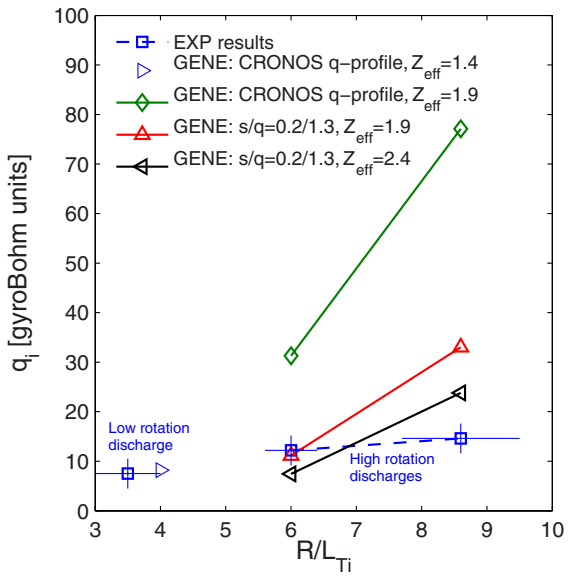

Figure 18. Comparison of nonlinear simulations and experimental results for the three separate discharges at $\rho = 0.33$. For the high rotation discharges, various sets of simulations with varying $\hat{s}$, q and Z_{eff} assumptions are shown. The GENE simulations corresponding to the low- and high-rotation discharges were carried out with $\gamma_E = 0.1$ and 0.3, respectively.

ion heat flux is only a factor of $\times 2.5$ above the experimental value, which is a discrepancy that can then be explained by a reasonable variation of input parameters around the experimental uncertainties. This inclusion of active fast ion species in the electromagnetic simulations, and the subsequent stabilization of the ITG turbulence, is a key factor for reconciling the experimental observations and the simulations.

From dedicated simulations, the fast ion stabilization was seen not to be an effective stabilizing factor for the high stiffness 73221 case, showing that this mechanism can separate the high and low-stiffness branches. This is due to the lower β and lower thermal and suprathermal pressure gradients in 73221 compared with 66404, reducing significantly the impact of the electromagnetic stabilization.

Table 4. Input data and ion-heat-flux results for discharge 66130 and 66404 nonlinear simulations. The cases in bold font are the simulations displayed in figure 18.

Shot number	$Z_{\rm eff}$	R/L_{Ti}	$T_{\rm e}/T_{\rm i}$	$\hat{s}$	q	$q_{\rm i}$ (gyroBohm units)
66130	1.4	6	1.25	0.2	1.3	19.4
66130	1.4	6	1.12	0.2	1.3	12.3
66130	**1.9**	**6**	**1.25**	**0.7**	**1.8**	**31.3**
66130	**1.9**	**6**	**1.25**	**0.2**	**1.3**	**11.1**
66130	**2.4**	**6**	**1.25**	**0.2**	**1.3**	**7.5**
66404	1.4	8.6	1.14	0.2	1.3	53.2
66404	**1.9**	**8.6**	**1.14**	**0.4**	**1.8**	**77.1**
66404	**1.9**	**8.6**	**1.14**	**0.2**	**1.3**	**33**
66404	2.4	8.6	1.14	0.4	1.8	47
66404	**2.4**	**8.6**	**1.14**	**0.2**	**1.3**	**23.8**
66404	2.4	7.7	1.08	0.2	1.3	13.7

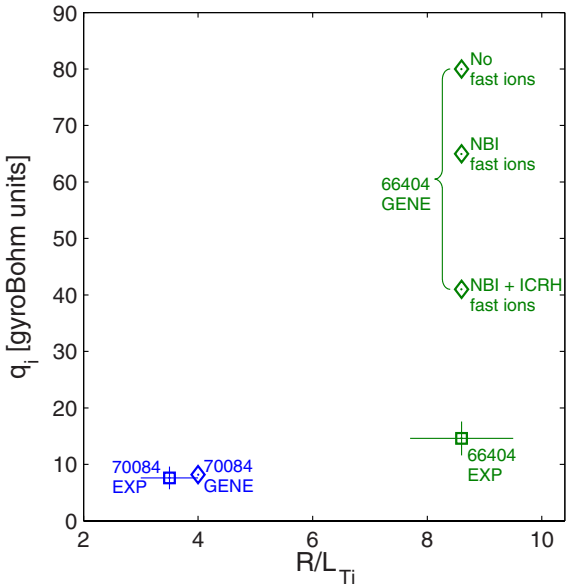

Figure 19. Comparison of measured heat flux and predicted values from electromagnetic simulations of discharge 66404 with: no fast ions (as shown in green in figure 18), NBI induced active fast ions, and both NBI + ICRH induced active fast ions (the nominal case). The 70084 measured and predicted ion heat flux is also shown for reference. The electromagnetic stabilization is enhanced by the fast ion pressure gradient and the fully nominal case is only ×2.5 above the experimental value.

Furthermore, EVE [62] simulations of the ICRH power deposition profile and associated suprathermal pressure show that the 73221 profile is significantly narrower than the 66404 case. This suggests that the 73221 suprathermal pressure may be negligible at the experimentally relevant $\rho = 0.33$ location, in line with the separation of the two branches. However, since EVE presently does not retain finite orbit width effects, it tends to underestimate the suprathermal pressure profile width. Nevertheless, we note that the electromagnetic stabilization effect is still weak even if we assume an overlap of the 73221 suprathermal pressure profile with the $\rho = 0.33$ location.

The predicted and experimental fluxes for 66404 can also be reconciled by both artificially increasing γ_E beyond the measured value from the toroidal rotation, and simultaneously ignoring PVG destabilization. This is shown in an additional set of simulations displayed in figure 20. This assumption

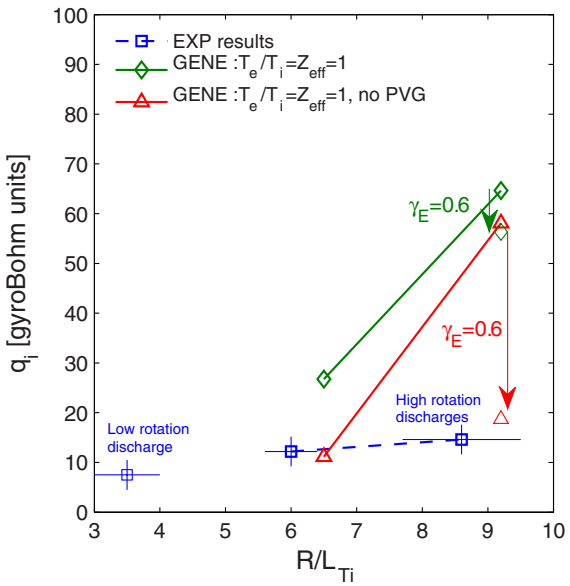

Figure 20. Comparison of flux values from nonlinear simulations and experimental power balance for the high-rotation discharges 66130 and 66404 at $\rho = 0.33$. Here we assumed for simplicity $T_{\rm e}/T_{\rm i} = Z_{\rm eff} = 1$. $\hat{s}/q = 0.2/1.3$ in these simulations. Sets of simulations both including and excluding the PVG drive are shown. For each set, additional 66404 simulations with γ_E increased from 0.3 to 0.6 were carried out.

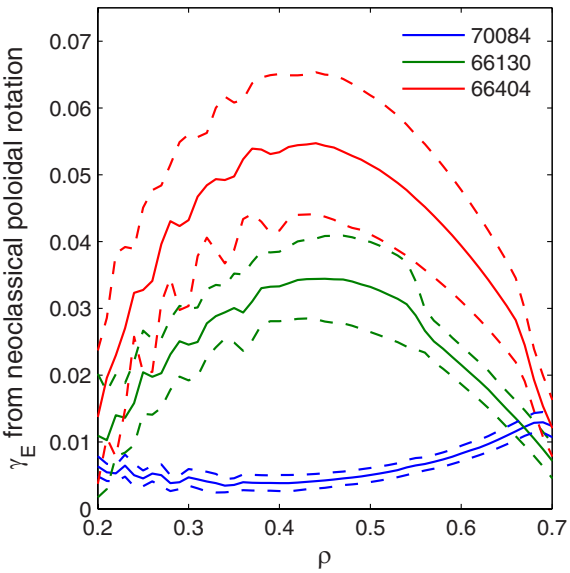

Figure 21. γ_E derived from the NCLASS predicted poloidal rotation for deuterium. The solid lines are the average values over the 1 s time window studied for each case. The dashed lines corresponded to the standard deviation of the profiles around the mean during the time window.

is consistent with assuming non-negligible poloidal rotation. However, our original assumption of negligible poloidal rotation due to neoclassical damping was justified according to NCLASS [63] neoclassical poloidal rotation predictions for the deuterium species within the CRONOS modelling. This is seen in figure 21, where the γ_E profiles derived from the NCLASS predicted poloidal rotation are shown. While there is an increase in γ_E correlated with increasing R/L_{Ti} as expected,

Table 5. Comparison of ion heat, electron heat, and electron particle fluxes for discharge 66404, including kinetic fast ions. All fluxes are in gyroBohm units. The errors in the power/particle balance signify statistical errors from the source modelling, and do not include any additional errors due to uncertainties in the background profiles.

Data source	q_i	q_e	Γ_e
GENE simulation	39 ± 9	21 ± 5	5.9 ± 1.6
Power/particle balance	14.3 ± 1.5	7.1 ± 0.9	0.35 ± 0.01

the absolute values are—while not entirely negligible for the 66130 and 66404 cases—still approximately an order of magnitude below the values necessary to provide significant turbulence suppression as observed. However, poloidal rotation values significantly above neoclassical values have been observed within internal transport barriers (ITBs) [64], and NCLASS predictions have also been shown to deviate from experimentally measured carbon and main ion poloidal rotation values at DIII-D [65, 66]. While we deem it unlikely that anomalous poloidal rotation is an important mechanism for flux reduction in the discharges we investigate here, in light of these observed discrepancies with neoclassical theory it is still nonetheless of interest to directly measure poloidal rotation in this class of low-stiffness-regime discharges, to examine whether any anomalous poloidal rotation is observed. It is also of interest to examine the extent to which theoretical mechanisms for generation of anomalous poloidal flow—potentially via a turbulent Reynolds stress—can play a role for cases with a high degree of external toroidal momentum injection.

Finally, while we have concentrated on analysis of the ion heat transport channel, we now briefly comment on the additional transport channels in discharge 66404, for the case including kinetic fast ions. The simulated and power/particle balance fluxes are compared in table 5. The Q_i/Q_e ratio agrees. However, the simulated electron outflux is an order of magnitude greater than the particle balance value, although this ratio difference is magnified by the globally smaller values of the particle flux compared with the heat fluxes. While factors such as R/L_{ne}, R/L_{Te}, and collisionality weakly impact the ion heat transport in our parameter range, they may have a significant impact on the particle transport. A sensitivity scan of these parameters within their confidence interval, which is particularly significant for R/L_{Te} and $R/_{ne}$, may shed light on this particle transport discrepancy. However, this further investigation of the particle transport is outside the scope of this work.

4.2.1. Summary of analysis at $\rho = 0.33$. We now summarize the entire discussion on the low-stiffness question. The predicted impact of the differences in parameters between the low-rotation discharge 70084 and the high-rotation discharges 66130 and 66404 at $\rho = 0.33$ were examined in detail with linear and nonlinear gyrokinetic simulations to investigate the potential factors leading to the observed reduced stiffness in the high-rotation cases. It was found that the differences in R/L_n and the effect of rotation on the equilibrium have negligible impact on the stiffness for our parameters. The effect of rotation itself, and the Shafranov shift stabilization due to suprathermal pressure in the high-rotation cases, have non-negligible but insufficient impact to explain the observed difference in rotation. The impact of q and $\hat{s}$ on the stiffness level is however significant. Finally, the nonlinear stabilization of ITG turbulence due to electromagnetic effects (β_e) was significant, reduces stiffness, and is further enhanced by including active fast ion species in the electromagnetic simulations.

When self-consistently including all effects, the ion heat flux values predicted by the gyrokinetic simulations agreed with the observed values in the low rotation case (70084), and were approximately $\times 2.5$ higher than the observed values for the high-rotation cases 66130 and 66404. For reasonable variations of the input parameters around their uncertainties, the simulated and experimental flux values for both 66130 and 66404 could be reconciled.

5. Simulated and measured ion-heat-flux comparisons at $\rho = 0.64$

In the previous section, the possible factors leading to a *difference* in stiffness between the low- and high-rotation discharges at $\rho = 0.33$ was investigated. In this section we investigate the experimental observation of a *lack* of stiffness reduction with rotation between the classes of discharges at $\rho = 0.64$, which attained similar R/L_{Ti} values, as seen in figure 1(*b*). Nonlinear simulations with GENE of three of the discharges were performed, with parameters matching those at $\rho = 0.64$. First, reduced simulations are carried out based on 70084 parameters, varying the rotation alone and examining its impact on R/L_{Ti} and the stiffness. Then, full simulations are carried out - analogous to those in section 4—and the GENE predicted ion heat fluxes are compared with the experimental values. For all the simulations is this section, the CRONOS calculated q and $\hat{s}$ values were taken for each discharge.

In figure 22 a nonlinear R/L_{Ti} scan with various levels of γ_E is shown. The scan is based on discharge 70084 parameters, but uses circular geometry, $\hat{s}/q = 2/3$, and is collisionless and electrostatic. The simulated stiffness is indeed greater than the $\rho = 0.33$ case shown in figure 5 as can be seen in a direct comparison shown in figure 23 for the $\gamma_E = 0$ case. Moreover, the degree of experimental γ_E variation between the discharges (between $\gamma_E = 0.1$–0.3) is also not sufficient to lead to a difference beyond typical error bars in R/L_{Ti}, for the same level of flux.

Examining the differences in experimental parameters for all 3 discharges between $\rho = 0.33$ and $\rho = 0.64$ in table 2, we can see that both $\hat{s}$ and q are higher at $\rho = 0.64$, and β_e is lower. All of these differences are expected to lead to higher stiffness in the $\rho = 0.64$ cases compared with $\rho = 0.33$. These qualitative differences in q-profile and β_e between low and high radii hold in general in tokamak discharges, apart from in special cases such as ITB discharges.

In figure 24, the full comparison between the simulations and the experiments is shown. These gyrokinetic simulations are electromagnetic, collisional, with numerical geometry, include a carbon species at a density consistent with $Z_{eff} = 1.9$ for 66130, and $Z_{eff} = 2.4$ for 70084 and 66404. The simulations include the experimental T_e/T_i. For all cases, the simulated and experimental ion heat flux agree approximately within 50%. This magnitude of difference can be easily reconciled within the reasonable uncertainties

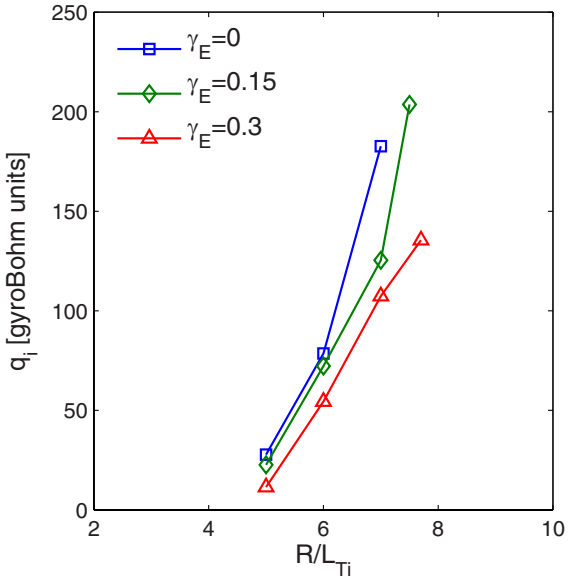

Figure 22. Nonlinear R/L_{Ti} scan for various levels of γ_E, based on the 70084 parameters at $\rho = 0.64$. Circular geometry, $\hat{s}/q = 2/3$, collisionless and electrostatic.

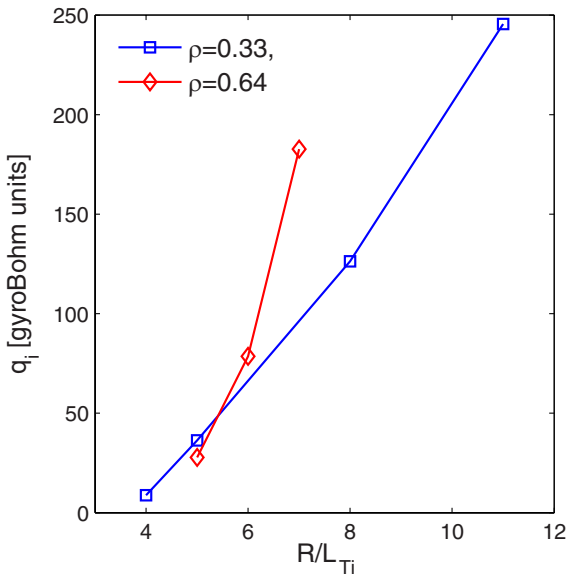

Figure 23. Nonlinear R/L_{Ti} scan comparing the stiffness level at $\rho = 0.33$ and $\rho = 0.64$, at $\gamma_E = 0$, based on the 70084 parameters. Circular geometry, collisionless, and electrostatic.

of input modelling parameters such as R/L_{Ti}, T_e/T_i or Z_{eff}, particularly for these stiff transport cases. Furthermore, the far off-axis ICRH driven suprathermal pressure profile was not included in the 70084 simulation, which may explain a proportion of the overprediction observed. An R/L_{Te} sensitivity check for discharge 66130 was carried out, which had the largest relative R/L_{Te} error throughout the data set, as seen in table 2. It was found from the dedicated nonlinear simulations that within the possible R/L_{Te} range the impact on ion heat transport is minimal.

To summarize, the effect of rotation alone at $\rho = 0.64$ is not expected to lead to experimentally discernible differences

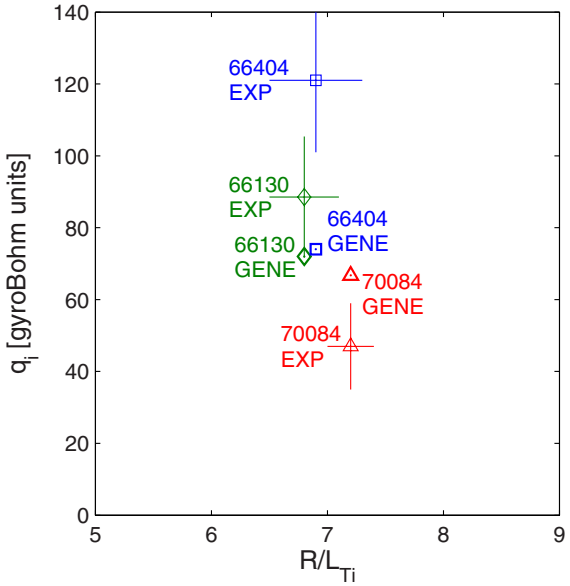

Figure 24. Comparison between gyrokinetic simulations and experiment at $\rho = 0.64$ for all three discharges. The experimental values (with the error bars) are shown for 70084 (red marker), 66130 (green marker) and 66404 (blue marker). The simulated values are shown with the same colour coding and marker style for all three discharges. Runs were electromagnetic, with collisions, and with numerical geometry.

in R/L_{Ti} and stiffness for the range of experimental γ_E examined. This is in agreement with the experimental trend seen in figure 1(*b*). When comparing the full nonlinear gyrokinetic ion-heat-flux predictions with the experimental values at $\rho = 0.64$, general agreement within reasonable input parameter uncertainties is seen for all the discharges, both at high and low rotation.

6. Conclusions

Observations at JET have shown evidence of reduced ion temperature profile stiffness correlated with low magnetic shear and increased flow shear. The same data-set has also raised questions regarding the experimental validation of the Dimits shift paradigm, and the low-rotation subset of discharges within this data-set seemed to display *higher* profile stiffness than expected from gyrokinetic simulations. These observations have motivated extensive nonlinear gyrokinetic simulations to investigate these questions. Simulations using the GENE code were carried out, with parameters based on a subset of these JET discharges. Transport sensitivity scans of various parameters that differed between the discharges - aside from rotation - were carried out, to assess potential mechanisms that may explain the observations. Full simulations including electromagnetic effects, numerical geometry, Z_{eff}, experimental T_e/T_i, and rotation were also performed at $\rho = 0.33$ (in the low-stiffness zone) and $\rho = 0.64$ for the discharges studied. The predictions were compared with the experimental results. The conclusions can be summarized as follows.

(1) No clear disagreement is observed between the experimentally observed turbulence R/L_{Ti} threshold and

the upshifted (Dimits shift) nonlinear threshold predicted by the gyrokinetic simulations. Previously reported results of such a disagreement in [6, 7] were found to be highly sensitive to the precise choice of q values used for the simulations. Recently improved data processing methodology has led to a revised q value leading to a simulated threshold value consistent with the experimental observation. However, a firm conclusion on this point is not justified considering the sensitivity of the results to both q and $\hat{s}$.

(2) For the low-rotation branch at $\rho = 0.33$ within the dataset studied, the previous observations of anomalous high stiffness compared with the gyrokinetic simulations is likely explained by a downshift in the ITG critical gradient due to higher T_e/T_i in the high flux cases. However, a firm conclusion in this regard is precluded by the high sensitivity of the critical gradient to q and $\hat{s}$, and thus to the q-profile uncertainties.

(3) The gyrokinetic predictions and experimental fluxes were compared at $\rho = 0.64$ for the three discharges. The experimental variation in flow shear between the discharges was not predicted to be sufficient to lead to a discernible difference in R/L_{Ti}—in agreement with the observations. The simulated and experimental ion heat fluxes for all examined discharges all agreed to within approximately 50%. This degree of discrepancy can be explained by reasonable variations of the input parameters within the experimental uncertainties.

(4) At $\rho = 0.33$, a study was carried out of the transport sensitivity to variations in R/L_n, $Z_{\rm eff}$, T_e/T_i, dilution due to fast ions, increased Shafranov shift due to suprathermal pressure, and the effect of rotation on the equilibrium. It was established that none of the above factors are sole mechanisms for the transition to the reduced stiffness regime. Their cumulative effect is however not negligible—particularly that of fast ions both through dilution and an increased Shafranov shift, and that of $Z_{\rm eff}$.

(5) The sensitivity of the transport to β_e was examined. It was established that even for the relatively low β_e values present in these discharges, the nonlinear electromagnetic ITG stabilization is significant. We emphasize that this electromagnetic stabilization mechanism is *distinct* from the Shafranov shift α-stabilization, which is a purely geometric effect. The electromagnetic stabilization, at least for $\beta_e < 0.48\%$, is a stiffness reduction as opposed to a threshold shift for discharge 66404. The nonlinear stabilization is significantly greater than the linear β_e stabilization, and may be related to the observed increased relative amplitude of zonal modes. Importantly, the effect is further enhanced by the addition of active fast ion species in the electromagnetic simulations, whose pressure gradients add to the electromagnetic coupling.

(6) For the nominal parameters for both the low- and high-rotation cases at $\rho = 0.33$, agreement between the gyrokinetic simulations and the experimental ion heat fluxes could be obtained within reasonable variations of the input parameters within their uncertainties. While the competition between parallel velocity gradient (PVG) destabilization and $E \times B$ stabilization can reduce the stiffness in the vicinity of the turbulence threshold, the predicted flux levels themselves are still significantly higher than the experimental values. The key factor for improved agreement for the high $R/L_{Ti} = 8.6$ case is obtained by electromagnetic stabilization. Thus, we conclude that electromagnetic stabilization enhanced by fast ions—not rotational flow shear—is the primary factor responsible for the low-stiffness regime. Since flow shear and fast ion content is typically coupled in NBI driven discharges, it is important to devise future experiments that decouple these effects for further investigation. In addition, further investigations of the parametrization of this effect is important for incorporation into the 'mixing length rule' of quasilinear transport formulations needed for predictive modelling. Attainment of high-β burning plasma scenarios is an aim for future devices such as ITER and DEMO. These devices are also expected to have a significant suprathermal pressure due to the α-particle fusion products. These results, whereby fast ions contribute to an electromagnetic ITG stabilization mechanism without increasing the underlying ITG drive, are likely to improve the extrapolation of scenarios to burning plasmas. This is of particular relevance to hybrid scenarios, which typically contain higher suprathermal pressure fractions than 'standard' scenarios owing to their reduced density, due to lower current.

Acknowledgments

This work, supported by the European Communities under the contract of Association between EURATOM/FOM and EURATOM/CEA, was carried out within the framework of the European Fusion Programme with financial support from NWO. The views and opinions expressed herein do not necessarily reflect those of the European Commission. This work is supported by NWO-RFBR Centre-of-Excellence on Fusion Physics and Technology (Grant nr 047.018.002). This work is part of the research programme 'Fellowships for Young Energy Scientists' (YES!) of the Foundation for Fundamental Research on Matter (FOM), which is financially supported by the Netherlands Organization for Scientific Research (NWO). The authors would like to thank: H. Doerk, D.R. Hatch, N. Hawkes, E. Highcock, F. Millitello, A. Schekochihin, M. Schneider, and E. Westerhof for stimulating discussions. Resources of HPC-FF in Jülich are gratefully acknowledged. This research used computational resources at the National Research Scientific Computing Center, which is supported by the Office of Science of the US Department of Energy under Contract No DE-AC02-05CH11231. The authors are grateful to D.R. Mikkelsen for assistance.

References

[1] Doyle E.J. *et al* 2007 Progress in the ITER Physics Basis: Chapter 2. Plasma confinement and transport 2007 *Nucl. Fusion* **47** S18
[2] Romanelli F. 1989 *Phys. Fluids* B **1** 1018
[3] Biglari H., Diamond P.H. and Rosenbluth M.N. 1989 *Phys. Fluids* B **1** 109
[4] Guo S.C. and Romanelli F. 1993 *Phys. Fluids* B **5** 520
[5] Diamond P., Itoh S.-I., Itoh K. and Hahm T.S. 2005 *Plasma Phys. Control. Fusion* **47** R35

[6] Mantica P. *et al* 2009 *Phys. Rev. Lett.* **102** 175002
[7] Mantica P. *et al* 2011 *Phys. Rev. Lett.* **107** 135004
[8] Mantica P. *et al* 2011 *Plasma Phys. Control. Fusion* **53** 124033
[9] Dimits A.M. *et al* 2000 *Phys. Plasmas* **7** 969
[10] Jenko F., Dorland W., Kotschenreuther M. and Rogers B.N. 2000 *Phys. Plasmas* **7** 1904
[11] Ryter F. *et al* 2011 *Nucl. Fusion* **51** 113016
[12] Artaud J.F. *et al* 2010 *Nucl. Fusion* **50** 043001
[13] Maggi C.F. *et al* 2010 *Nucl. Fusion* **50** 025023
[14] Brizard A.J. and Hahm T.S. 2007 *Rev. Mod. Phys.* **79** 421–68
[15] Lapillonne X. *et al* 2009 *Phys. Plasmas* **16** 032308
[16] Beliën A.J.C., Botchev M.A., Goedbloed J.P., van der Holst B. and Keppens R. 2002 *J. Comput. Phys.* **182** 91–117
[17] Candy J., Waltz R.E. and Dorland W. 2004 *Phys. Plasmas* **11** L25
[18] McMillan B.F. *et al* 2010 *Phys. Rev. Lett.* **105** 155001
[19] Kammerer M., Merz F. and Jenko F. 2008 *Phys. Plasmas* **15** 052102
[20] Merz F., Kowitz C., Romero E., Roman J.E. and Jenko F. 2012 *Comput. Phys. Commun.* **183** 922
[21] Candy J. and Waltz R. 2003 *J. Comput. Phys.* **186** 545
[22] Jenko F., Dorland W. and Hammett G.W. 2001 *Phys. Plasmas* **8** 4096
[23] Citrin J. *et al* 2012 *Phys. Plasmas* **19** 062305
[24] Dannert T. and Jenko F. 2005 *Phys. Plasmas* **12** 072309
[25] Hirose A., Livingstone S. and Singh A.K. 2005 *Nucl. Fusion* **45** 1628
[26] Kinsey J.E., Waltz R.E. and Candy J. 2006 *Phys. Plasmas* **13** 022305
[27] Kotschenreuther M. *et al* 1995 *Comput. Phys. Commun.* **88** 128
[28] Brix M., Hawkes N.C., Boboc A., Drozdov V. and Sharapov S.E. 2008 *Rev. Sci. Instrum.* **79** 10F325
[29] Mikkelsen D.R. and Dorland W. 2008 *Phys. Rev. Lett.* **101** 135003
[30] Burrell K.H. 1997 *Phys. Plasmas* **4** 1499
[31] Terry P.W. 2000 *Rev. Mod. Phys.* **72** 109
[32] Waltz R.E., Kerbel G.D. and Milovich J. 1994 *Phys. Plasmas* **1** 2229
[33] Waltz R.E., Kerbel G.D., Milovich J. and Hammett G.W. 1995 *Phys. Plasmas* **2** 2408
[34] Waltz R.E., Candy J.M. and Rosenbluth M.N. 2002 *Phys. Plasmas* **9** 1938
[35] Kinsey J.E., Waltz R.E. and Candy J. 2005 *Phys. Plasmas* **12** 062302
[36] Roach C.M. *et al* 2009 *Plasma Phys. Control. Fusion* **51** 124020
[37] Catto P.J., Rosenbluth M.N. and Liu C.S. 1973 *Phys. Fluids* **16** 1719
[38] Newton S.L., Cowley S.C. and Loureiro N.F. 2010 *Plasma Phys. Control. Fusion* **52** 125001
[39] Dimits A.M., Cohen B.I., Nevins W.M. and Shumaker D.E. 2001 *Nucl. Fusion* **40** 1725
[40] Highcock E.G. *et al* 2010 *Phys. Rev. Lett.* **105** 215003
[41] Huysmans G.T.A., Goedbloed J.P. and Kerner W. 1991 *CP90 Conf. on Computational Physics (Amsterdam, The Netherlands, Sept. 1990)* (Singapore: World Scientific) p 371
[42] Merz F. and Jenko F. 2010 *Nucl. Fusion* **50** 054005
[43] Tardini G. *et al* 2007 *Nucl. Fusion* **47** 280
[44] Bourdelle C. *et al* 2005 *Nucl. Fusion* **45** 110
[45] Romanelli M., Zocco A., Crisanti F. and JET-EFDA Contributors 2010 *Plasma Phys. Control. Fusion* **52** 045007
[46] Holland C. *et al* 2011 *Phys. Plasmas* **18** 056113
[47] Schneider M. *et al* 2011 *Nucl. Fusion* **51** 063019
[48] Hedin J., Hellsten T., Eriksson L.-G. and Johnson T. 2002 *Nucl. Fusion* **42** 527
[49] Pueschel M.J., Kammerer M. and Jenko F. 2008 *Phys. Plasmas* **15** 102310
[50] Weiland J. and Hirose A. 1992 *Nucl. Fusion* **32** 151
[51] Hirose A. 2000 *Phys. Plasmas* **7** 433
[52] Pueschel M.J. and Jenko F. 2010 *Phys. Plasmas* **17** 062307
[53] Chen Y. *et al* 2003 *Nucl. Fusion* **43** 1121
[54] Candy J. 2005 *Phys. Plasmas* **12** 072307
[55] Pueschel M.J. *et al* 2013 *Phys. Rev. Lett.* **110** 155005
[56] Pueschel M.J., Görler T., Jenko F., Hatch D.R. and Cianciara A.J. 2013 *Phys. Plasmas* **20** 102308
[57] Militello F., Romanelli M., Connor J.W. and Hastie R.J. 2011 *Nucl. Fusion* **51** 033006
[58] Jiquan L. and Kishimoto Y. 2005 *Phys. Plasmas* **12** 054505
[59] Migliano P. *et al* 2013 *Plasma Phys. Control. Fusion* **55** 055003
[60] Holland C. *et al* 2012 *Nucl. Fusion* **52** 114007
[61] Citrin J. *et al* 2013 *Phys. Rev. Lett.* **111** 155001
[62] Dumont R.J. 2009 *Nucl. Fusion* **49** 075033
[63] Houlberg W.A., Shaing K.C., Hirshman S.P. and Zarnstroff M.C. 1997 *Phys. Plasmas* **4** 3230
[64] Crombé K. *et al* 2005 *Phys. Rev. Lett.* **95** 155003
[65] Solomon W.M. *et al* 2006 *Phys. Plasmas* **13** 056116
[66] Grierson B.A. *et al* 2012 *Phys. Plasmas* **19** 056107